bioRxiv preprint doi: https://doi.org/10.1101/2021.10.11.463968; this version posted October 11, 2021. The copyright holder for this preprint (which was not certified by peer review) is the author/funder, who has granted bioRxiv a license to display the preprint in perpetuity. It is made available under aCC-BY-NC-ND 4.0 International license.

The spatial organization of replication is determined by cell size independently of chromosome copy number

Anna Knöppel[1]*, Oscar Broström[1]*, Konrad Gras[1], David Fange[1#] & Johan Elf[1#]
* Equal contribution
[#] Corresponding authors: david.fange@icm.uu.se & johan.elf@icm.uu.se
[1] Department of Cell and Molecular Biology, Science for Life Laboratory, Uppsala University, Uppsala, Sweden

Abstract

We have studied how *Escherichia coli* coordinates replication and division cycles by tracking replisomes in individual cells through thousands of division cycles. By analysing the replication and division of the cells at various growth rates and with different genetic perturbations, we have reached four major conclusions: (1) Initiation is not based on titration of DnaA to the chromosomal binding sites because initiation is still coordinated with the division cycle several generations after DnaA synthesis is turned off. (2) We can rule out that initiation is triggered by a simple DnaA-ADP/ATP switch mechanism because initiation is still triggered at a well-defined cell size in a *DARS1/DARS2/datA* triple knockout if DnaA is overexpressed. (3) From the spatial organization of replisomes at different growth rates, it appears as if initiation is triggered by termination, but this hypothesis is ruled out by an NGS-based marker frequency analysis. (4) Overlapping replication cycles do not affect the spatial organization of the replication machinery and it appears as if each replication center contains a fixed number of DnaN molecules independently of how many replication forks are being processed.

Introduction

The ambition of this work has been to discover how *Escherichia coli* triggers replication initiation to coordinate DNA replication with cell growth. This is a classical field of study which has been approached from different directions. Through the mechanistic genetic/biochemical path, a number of mechanisms that contribute to regulation have been described. These include *e.g.* the critical role of DnaA-ATP for initiating replication at *oriC* (Hansen and Atlung, 2018), autoregulation of DnaA expression (Hansen and Rasmussen, 1977), sequestration of *oriC* just after initiation to prevent over initiation (Campbell and Kleckner, 1990), binding of DnaA to DnaA boxes throughout the chromosome (Schaper and Messer, 1995), and the DnaA-ATP ⇔ DnaA-ADP conversion. The latter includes *e.g.* the importance of *hda*-regulated inactivation of DnaA (RIDA) (Katayama et al., 1998; Kurokawa et al., 1999; Kasho and Katayama, 2013; Kitagawa et al., 1996), and the chromosomal loci

bioRxiv preprint doi: https://doi.org/10.1101/2021.10.11.463968; this version posted October 11, 2021. The copyright holder for this preprint (which was not certified by peer review) is the author/funder, who has granted bioRxiv a license to display the preprint in perpetuity. It is made available under aCC-BY-NC-ND 4.0 International license.

DARS1, DARS2, and datA (Fujimitsu and Katayama, 2004; Kasho and Katayama, 2013). It is, however, still not known how these systems operate together to regulate replication initiation, *i.e*. to trigger initiation when there is too little DNA compared to the cell mass.

There is also a more recent, phenomenological, path that has emerged from the breakthroughs in live-bacterial imaging, initiated by the invention of the mother machine microfluidic chip (Wang et al., 2010). This path was initially focused on statistical properties of cell-size variation from generation to generation because this was what could be measured with phase-contrast microscopy alone (Amir, 2014; Campos et al., 2014; Taheri-Araghi et al., 2015). It was however clear that these studies could only define limits that the mechanistic models should satisfy; it is important to complement the imaging studies with molecular reporters, for example by tracking the replication forks and the division cycles at the same time with fluorescence microscopy (Si et al., 2019; Wallden et al., 2016). Earlier, chromosome tracking over the cell cycle was pioneered in a low throughput setting (Bates and Kleckner, 2005; Lau et al., 2003; Li et al., 2002). Here, we combine the two paths and study replication and division cycles using high-throughput fluorescence microscopy while at the same time perturbing the system to gain insights on the importance of each component.

Mechanisms for balancing replication initiation to cell growth

The cell triggers a new round of replication on each origin once per generation, on average. It also seems to keep the ratio of chromosomal DNA to protein within 25% independently of growth rate and cell size (Dennis and Bremer, 1974). There are at least four principally different ways suggested for achieving this level of regulation, all depending on triggering replication when there is too little DNA compared to the cell size.

Inhibitor dilution: In this hypothetical mechanism, each copy of the genome expresses a constant number of replication inhibitors per time, *i.e.* expression is limited by transcription and not translation and the concentration of RNA polymerase is constant. The inhibitors are diluted by growth such that initiation is triggered when the repressor concentration drops below a specific value. This mechanism would rely on a very sensitive concentration dependence for the repression and would be exceptionally sensitive to noise in gene expression. A similar model was proposed by (Pritchard et al., 1969), but here a fixed number of inhibitors are made for each replication event and then these are diluted by growth. We will not investigate this mechanism further since no such inhibitor is known.

Activator titration: In this type of model, the activator is kept at a constant concentration in the cell. Therefore, the number of activator molecules increases as the cell grows in size. The activators can bind strongly to a fixed number of sites per chromosome. When the sites are full, excess synthesis contributes to increasing the concentration of free activators, and thus, initiation is triggered at a fixed volume per chromosome in each generation. This model could in principle be implemented by the binding of DnaA to chromosomal DnaA boxes. The activator titration model predicts that an increased expression of DnaA would shift initiation to smaller volumes and that more DnaA boxes would delay initiation (Christensen et al., 1999; Hansen et al., 1991).

bioRxiv preprint doi: https://doi.org/10.1101/2021.10.11.463968; this version posted October 11, 2021. The copyright holder for this preprint (which was not certified by peer review) is the author/funder, who has granted bioRxiv a license to display the preprint in perpetuity. It is made available under aCC-BY-NC-ND 4.0 International license.

DnaA-ATP/ADP titration: In this class of models, initiation is triggered by the concentration of DnaA-ATP or the DnaA-ATP/DnaA-ADP ratio *(Donachie and Blakely, 2003).* The regulation works most effectively if DnaA-ATP is converted to the ADP-form in proportion to the number of chromosomes, and back to the ATP-form in proportion to the cell size (Wallden et al., 2016). The most important molecule converting DnaA-ATP into DnaA-ADP is Hda, which is the key component of RIDA. RIDA, in turn, depends on actively replicating DNA polymerases to exert its function. However, there are no known molecules capable of converting DnaA back to the ATP state proportionally to cell size. We will discuss this further below.

Mechanical models: There is also a class of initiation models that depend on triggering replication based on other processes in the cell cycle. This effectively moves the regulatory problem to these other processes. For example, if replication is triggered after cell division, the challenge is not to initiate at a set size, but to divide at a set size. One can also envision triggering replication by replication termination, which moves the regulatory problem to replicating the chromosome at a rate that is proportional to the growth rate. We will revisit this possibility.

Results

Experimental setup and data visualization

Our typical experimental procedure for studying replication in relation to the cell cycle is to grow *E. coli* MG1655 cells in a mother machine type fluidic chip that allows rapid media switches (Baltekin et al., 2017). We used this strategy to monitor thousands of individual cell cycles in each experiment. The cells were grown at 30 °C in M9 minimal medium supplemented with a carbon source and 1×RPMI amino acids solution unless otherwise stated. The growth medium is referred to only by the name of the carbon source; precise media compositions can be found in Table S1. The growth was imaged by phase contrast and the replication forks were localized by detecting the fluorescence of YFP fusions to DnaQ, DnaN or SeqA. DnaQ and DnaN are both part of the replisome and SeqA binds hemimethylated GATC in the wake of the complex. The different replication markers gave very similar information (Figure S1A). We regularly present the output as “fork plots" (Camsund et al., 2020), depicting the distribution of replisomes along the long axis of the cells for each cell size (Figure 1A). The highly occupied regions in the fork plots are referred to as branches. In Figure 1A, the beginning and the end of these branches are spatially distinct. We interpret the beginning of each branch as the initiation of individual rounds of DNA replication with two replication forks moving bidirectionally away from the origin region. The end of each branch is interpreted as the termination of the round of replication that was initiated at the beginning of the branch. We discuss this interpretation later in the text. The fork plots also typically indicate the average cell size at birth and division with dashed white lines. The methods section describes how these quantities were defined and calculated, but importantly, the individual replication forks were tracked in time (Figure 1B) such that, for example, replication initiation could be automatically assigned based on when the trajectories start unless otherwise stated.

bioRxiv preprint doi: https://doi.org/10.1101/2021.10.11.463968; this version posted October 11, 2021. The copyright holder for this preprint (which was not certified by peer review) is the author/funder, who has granted bioRxiv a license to display the preprint in perpetuity. It is made available under aCC-BY-NC-ND 4.0 International license.

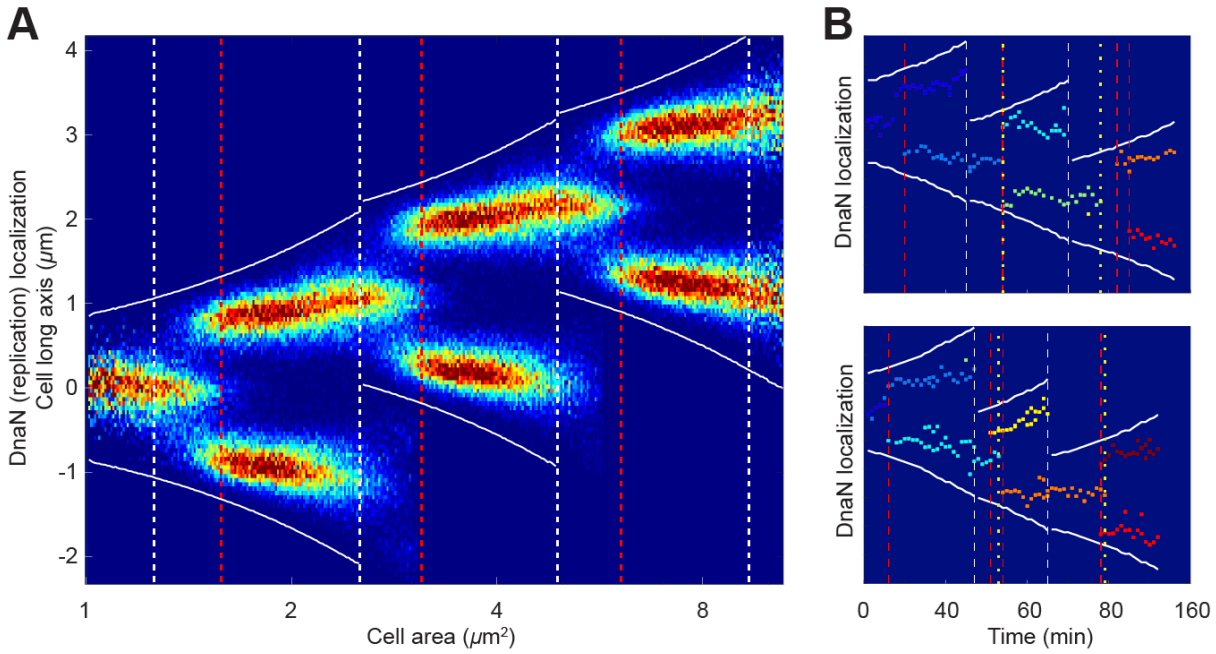

Figure 1. Example figures for bulk and single cells. *(**A**) Three generation fork plot, i.e a two-dimensional distribution of position of YPet-DnaN foci along the long-axis of the cells (y-axis) and cell size (x-axis). Here, the cell size in generation two and three are defined as if the cell in generation one had not divided. Dashed white horizontal lines indicate the average sizes of cells at birth or division. Dashed horizontal red lines indicate the median initiation size as determined by tracking replisomes in single cells. Solid white lines indicate average cell pole positions. (**B**) Two examples of detected YPet-DnaN foci as function of time for cells that have been tracked for at least three division events. Dots with the same color have been linked together into a track using u-track (Jaqaman et al., 2008). The lines are the same as in A except the red dashed lines now indicate replication initiation times and yellow spotted lines indicate termination of replication (criteria for determining these can be found in the methods section).*

Initiation of DNA replication can be triggered both in the absence of DnaA gene expression and of its transcriptional regulation

DnaA is known to negatively control its own transcription (Hansen and Atlung, 2018). To investigate whether this feedback plays a crucial role in triggering replication initiation, we constructed a strain in which the expression of a sole copy of *dnaA* is constitutive. This was done by introducing *dnaA* under the control of a constitutive promoter (J23106) at a neutral position and exchanging the two native promoters of the *dnaA* operon as well as the *dnaA* gene with a constitutive promoter (J23106), which was placed in front of the remaining of the operon (*dnaN*, *recF* and *gyrB*). The strain EL558 with constitutive *dnaA* expression showed a very similar average expression of DnaA as compared to wt (3% difference by MS and 1% by RT-qPCR; Figure S2) and a minor increase in average initiation (EL558: 1.83 ± 0.094; EL562: 1.77 ± 0.068) and average division sizes (EL558: 3.485 ± 0.268; EL562: 2.995 ± 0.202) (Figure 2A; Figures S3–S5). Errors are standard deviations of 6 or 11 experiments, respectively. EL558 displayed an indistinguishable growth rate compared to an isogenic reference strain, both when grown in the microfluidics and in a plate reader (Figures S2 and S3). The two strains also generated very similar fork plots (Figure 2A; Figure S3) while the

bioRxiv preprint doi: https://doi.org/10.1101/2021.10.11.463968; this version posted October 11, 2021. The copyright holder for this preprint (which was not certified by peer review) is the author/funder, who has granted bioRxiv a license to display the preprint in perpetuity. It is made available under aCC-BY-NC-ND 4.0 International license.

strain with constitutive *dnaA* expression showed a modest increase in cell-to-cell variability of initiation sizes. The spread of the initiation size distribution for single cells increased from a coefficient of variation (CV) of 0.118±0.0157 in the wt strain to 0.106±0.0060 in the strain with constitutive expression. Errors are standard deviations of 6 or 11 experiments, respectively. Taken together, we concluded that the possibility of DnaA to control its own expression does not have a critical role in the regulation of replication initiation.

The non-critical effect of removing DnaA's transcriptional autoregulation allowed us to modify the DnaA expression level by exchanging the J23106 promoter in front of *dnaA* to other constitutive promoters or to the IPTG controllable *lac* promoter. We found that the initiation size divided by the number of origins on which initiation occurred correlated negatively with DnaA expression both for the IPTG inducible strain (Figure 2B) and for the different constitutive promoters (Figure 2A). Conversely, the increased DnaA expression had no significant effect on growth rate or cell size (Figure S2 and S3). A two-fold increase in DnaA concentration mediated by the J23100 promoter did not affect the cell-to-cell variability in initiation size. However, at even higher expression levels of DnaA (achieved by introducing the J23101b promoter; Figure 2A; Figure S3), we observed a significant increase in variability in initiation size. In addition, the J23101b carrying strain also showed dramatic increase in asynchrony as compared to wt (Figure S2), which is in line with what has been reported previously (Atlung and Hansen, 1993). We note that it is necessary to carefully interpret the rif-runout experiments in the DnaA-overexpressing strains (Figure S2) given the recent report that excess DnaA can trigger initiation even in the presence of rifampicin (Riber and Lobner-Olesen, 2020).

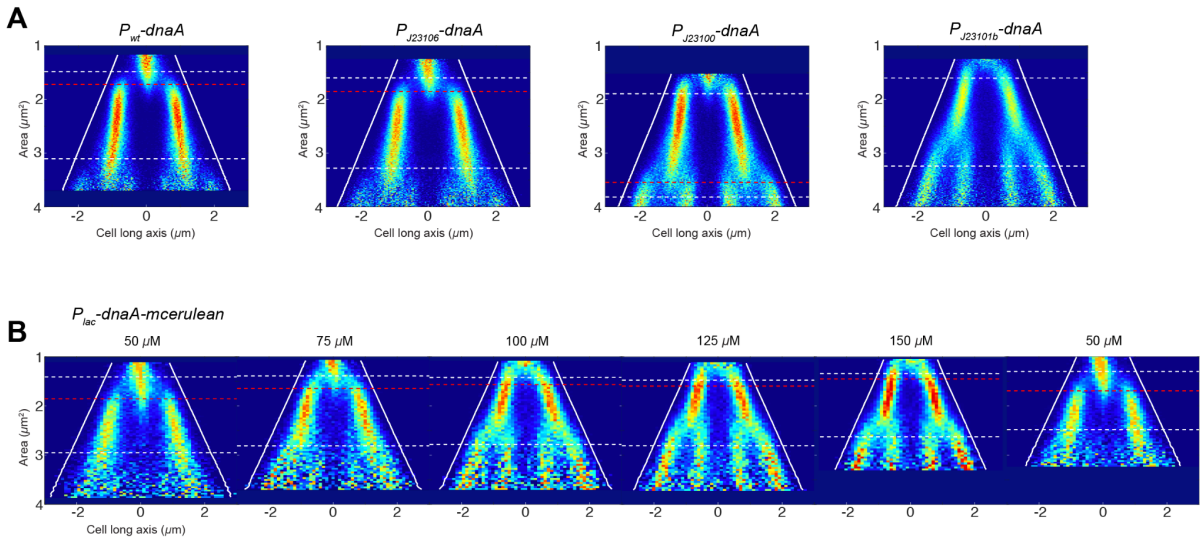

Figure 2. Fork plots for different levels of DnaA expression. *(**A**) Example fork plots for SeqA-Venus in strains carrying either the native promoter of dnaA (P_{wt}-dnaA), a constitutive promoter with the same DnaA expression level (P_{J23106}-dnaA), and two strains with higher expression levels as compared to wt (P_{J23100}-dnaA and $P_{J23101b}$-dnaA). (**B**) Example fork plots for SeqA-Venus in strains carrying the IPTG controllable P_{lac} promoter in front of dnaA (P_{lac}-dnaA-mCerulean) from an experiment in which the IPTG concentration in the growth medium is changed stepwise. IPTG concentrations after the switch are given above each fork plot. The cells were grown in succinate medium at 30 °C. White dashed lines correspond to average birth and division sizes, the red dashed line corresponds to the average initiation size from a Gaussian fit in (**A**) or bulk determination in (**B**) (see the methods section for details) and the white solid lines indicate the average cell pole position.*

bioRxiv preprint doi: https://doi.org/10.1101/2021.10.11.463968; this version posted October 11, 2021. The copyright holder for this preprint (which was not certified by peer review) is the author/funder, who has granted bioRxiv a license to display the preprint in perpetuity. It is made available under aCC-BY-NC-ND 4.0 International license.

The fact that the DnaA expression can change the initiation size, would be compatible with the activator titration model (Christensen et al., 1999; Hansen et al., 1991). To test this specific model, we measured if new synthesis of DnaA is needed for replication initiation. We used a strain (EL1548) with a single copy of *dnaA* under the control of the *lac* promoter and transcriptionally fused to the fluorescent protein mCerulean (Figures S6 and S7). This strain was used in experiments where DnaA expression was stopped, allowing the DnaA protein to be diluted by growth, while imaging both SeqA-Venus localization and mCerulean abundance (Figure 3). The dilution rate of mCerulean (56 min) corresponded to the growth rate in the replication experiment (49 min) and independant qPCR measurements of the *dnaA* transcript before and after removing IPTG shows that *dnaA* is effectively turned off when IPTG is removed (Figure S6). Additionally, LC MS/MS measurements of DnaA abundance suggested a two-fold lower decay rate compared to the imaging experiment (Table S2). However, we consider the qPCR results and the mCerulean dilution rates obtained from the same cells as the replication imaging experiment to be more reliable and we therefore conclude that DnaA expression is stopped when removing IPTG.

When DnaA was overexpressed, the cells initiated replication at a smaller size to chromosome ratio as compared to wt cells. As the DnaA concentration decreased by dilution, the cells gradually initiated replication at larger and larger size to chromosome ratios. The latter was evident up until the point where initiation stopped approximately at the wt concentration of DnaA. Based on initiation sizes, DnaA was diluted to wt levels 160–220 min after IPTG was removed from the medium (Figures 3A and 3B; repeat experiment Figure S8). Importantly, also after DnaA synthesis was stopped, cells were able to initiate replication for three or four generations in the same cell lineage (Figures 3C and 3D). During this time, mCerulean was diluted sixfold while initiations continued (Figure 3E). These results rule out activator titration models for replication initiation, since new initiation occurs even when no new DnaA is expressed.

Additionally, models where DnaA is in equilibrium between free or DNA bound states and the free concentration drives initiation cannot produce regular initiations after DnaA expression is turned off. This is because in cases with a fixed number of DnaA molecules, the model cannot result in a situation where the free concentration of DnaA is higher at larger volumes than at smaller. Although the number of free DnaA molecules increases with volume, the free concentration of DnaA will decrease monotonously with increasing volume. This is true irrespective of any cooperativity in binding to the DnaA boxes since the probability to find a DnaA in the bound state will increase monotonously with the free concentration. Taken together, this implies that as the volume increases, the free concentration cannot increase at the expense of a lower fraction bound.

bioRxiv preprint doi: https://doi.org/10.1101/2021.10.11.463968; this version posted October 11, 2021. The copyright holder for this preprint (which was not certified by peer review) is the author/funder, who has granted bioRxiv a license to display the preprint in perpetuity. It is made available under aCC-BY-NC-ND 4.0 International license.

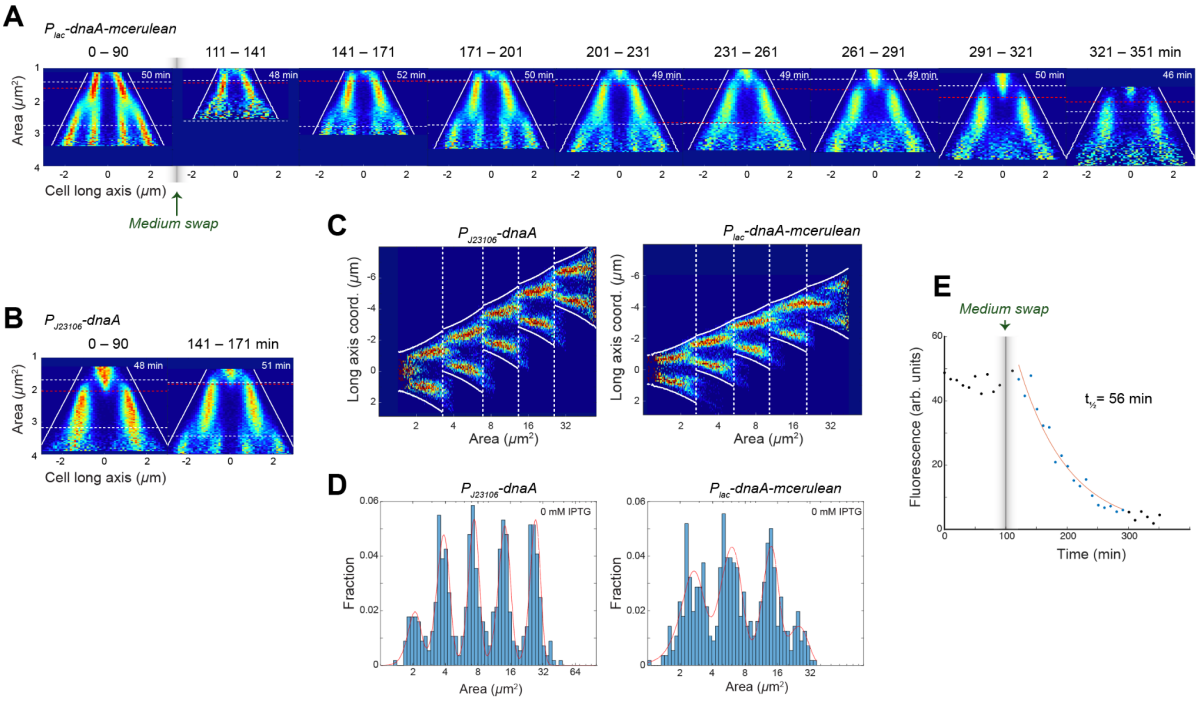

Figure 3. Initiations after turning off expression of DnaA. (A) *Fork plots for a strain with IPTG controllable DnaA expression (P_{lac}-dnaA-mCerulean) before (0–90 min) and after (111–351 min) the switch from media with 1 mM IPTG to media without IPTG. The media was switched manually and was finished 1 min before imaging was resumed (see detailed procedure in the methods section). In the analysis cells are required to have a parent and daughters living for 6 minutes. As a consequence the first (111–141 min) and the last (321–351 min) contain less data compared to the other fork plots. Lines and numbers as in Figure 2.* ***(B)*** *As in (A) but for a strain with constitutive expression of DnaA (P_{J23106}-dnaA) grown in the same microfluidic device. Only one representative fork plot after the switch to media without IPTG is shown (141–171 min).* ***(C)*** *Five generation fork plot after the switch to media without IPTG (111–351 min) for constitutive (left) and IPTG regulated (right) dnaA expression.* ***(D)*** *Distribution of single-cell initiation areas (blue bars) of the same cells as in C. Cells were a part of the same lineage. Red lines show the result of a regression of the distribution to either a sum of five (left) or a sum of four (right) Gaussians.* ***(E)*** *Mean of the per cell mCerulean fluorescence intensity area density as a function of time both before and after the media switch. Background fluorescence from cells not expressing mCerulean were subtracted from each cell intensity density. In each time-point a new set of cells was imaged to avoid the effect of photobleaching. Time-points after the media switch (blue) were fitted to a single exponential decay (red). The half-time of the exponential decay is 56 min. Lines and size definitions as in Figure 2B.*

The effects of the DnaA ADP/ATP ratio

Since the absolute DnaA concentration does not seem to be critical for the control of initiation, *i.e.* keeping the cell-to-cell variation in initiation sizes low, we next quantified the role of the known regulators of the DnaA-ATP/ADP conversion (Figure 4). In the strain expressing DnaA constitutively from the J23106 promoter, we made marker- and scar-free deletions of the *DARS1*, *DARS2, and datA* loci, as well as combinations of double and triple knockouts. *DARS1* and *DARS2* are known to contribute to the DnaA-ADP to DnaA-ATP conversion (Fujimitsu and Katayama 2004), whereas *datA* contributes to the DnaA-ATP to DnaA-ADP conversion (Kasho and Katayama 2013).

As expected, replication initiation occurred in smaller-sized cells when a negative regulator of conversion to the DnaA-ATP state was removed (*datA*), and in larger-sized cells when a

bioRxiv preprint doi: https://doi.org/10.1101/2021.10.11.463968; this version posted October 11, 2021. The copyright holder for this preprint (which was not certified by peer review) is the author/funder, who has granted bioRxiv a license to display the preprint in perpetuity. It is made available under aCC-BY-NC-ND 4.0 International license.

positive regulator was removed (*DARS1*) (Figure 4B). Also, removal of *DARS2* resulted in slightly larger initiation volumes compared to the reference strain in the same experiment (Figure S4).

Our results are in partial conflict with previously published results. It has been described that deleting *DARS2* gives a more severe effect on replication initiation than deleting *DARS1*, and deleting *DARS2* or *datA* is described to lead to asynchronous replication initiation whereas deleting *DARS1* is not (Katayama et al., 2017). Our data suggest the opposite: Δ*DARS1* gave a more severe regulatory phenotype than Δ*DARS*2 in terms of cell-to-cell variation in replication initiation size, and Δ*DARS1* increased asynchrony while Δ*DARS2* or Δ*datA* did not (Figure S4). The three mutants have also been whole-genome sequenced, confirming the intended mutations. Interestingly, Δ*datA* could ameliorate the effects of Δ*DARS1* both when it came to replication initiation sizes and the increased variation in replication initiation sizes. Even the triple mutant Δ*DARS1* Δ*DARS2* Δ*datA* does not display any growth defect, *i.e*. it initiates every generation, although it was inaccurate in replication initiation size control.

To rule out the possibility that the deletions act differently in the *dnaA* constitutive background as compared to *dnaA* wt background, we also tested such constructs (Figure 4C; Figure S5). Δ*DARS1* still displayed a more severe phenotype as compared to Δ*DARS2,* but the effect was smaller than in the background of the constitutive *dnaA* expression, presumably because DnaA expression is upregulated to compensate for the reduced concentration of DnaA-ATP. On its own, it appears as if the DnaA-ADP to ATP conversion activity conferred by *DARS1* is important to reach the initiation potential at a well-defined size.

We also intended to investigate the effect of Hda on replication initiation sizes. Hda mediates conversion of DnaA-ATP to DnaA-ADP as a consequence of ongoing replication (Kato and Katayama 2001). We were not able to delete *hda*, presumably due to it being crucial for cell viability. However, we have previously observed highly variable initiation sizes in a *hda* CRISPR knockdown (Camsund et al., 2020) and we also observe that overexpression of *hda* does give the expected effect of initiation at a larger size, as a consequence of excessive removal of DnaA-ATP (Figure 4D).

DnaA in the ATP form is essential to initiate replication (Sekimizu et al., 1987). At the same time, we found that initiation still works in the *DARS1*:*DARS2*:*datA* triple knockout that is expected to be unable to convert the ADP form into the ATP form. In this context, we do not consider the possibility of DnaA-ATP to DnaA-ADP conversion by acidic phospholipids since we did not see any phenotype for *pgsA* in a previous CRISPR screen (Camsund et al., 2020). We therefore tested if DnaA-ATP arises from new synthesis of DnaA. Using an IPTG-inducible *dnaA* construct in the triple knockout background, we found that there are multiple new rounds of replication initiated after synthesis of DnaA is stopped also in this case (Figures 4E–G). As a consequence, we conclude that if DnaA-ATP is needed for initiation, there is a hitherto unknown mechanism to convert DnaA to the ATP form. Furthermore, it is also clear that overexpression of DnaA seemingly ameliorates the deleterious effects of the triple mutant with respect to the cell-to-cell variation in initiation size, suggesting that the mutant simply has too little DnaA-ATP and not that the *DARS* and *datA* sites are critical for the control as such.

bioRxiv preprint doi: https://doi.org/10.1101/2021.10.11.463968; this version posted October 11, 2021. The copyright holder for this preprint (which was not certified by peer review) is the author/funder, who has granted bioRxiv a license to display the preprint in perpetuity. It is made available under aCC-BY-NC-ND 4.0 International license.

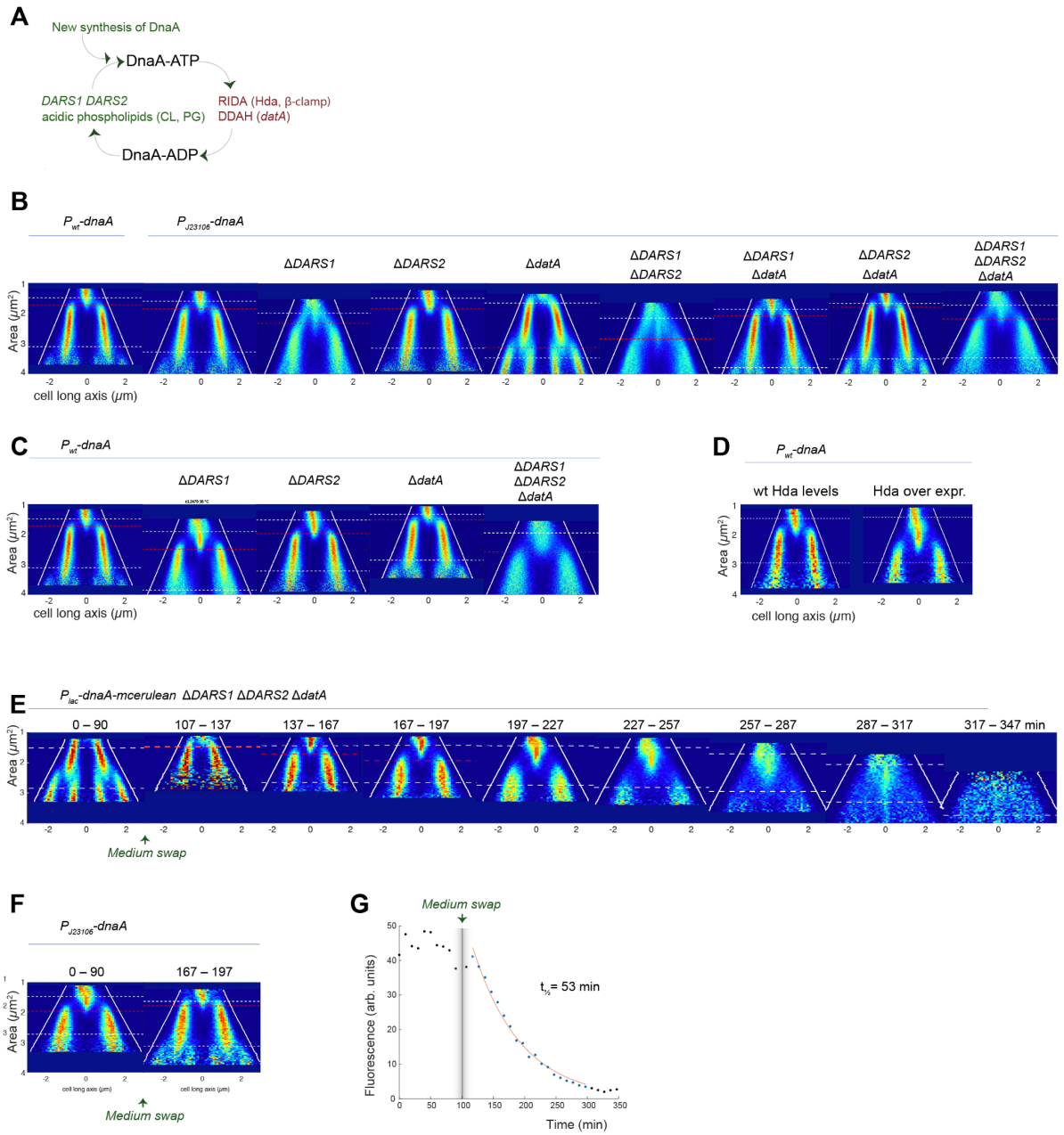

Figure 4. Replication phenotypes of DnaA-ATP/ADP regulatory mutants. *(**A**) Cartoon of DnaA-ATP/ADP regulation. Multiple systems can convert between the two DnaA forms. Green = positive regulators and red = negative regulators. (**B**–**D**) Fork plots of DnaA-ATP/ADP regulation mutants. (**B**) knockout mutations made in the background of P_{J23106}-dnaA. (**C**) knockouts in P_{wt}-dnaA background. (**D**) Hda overexpression driven by P_{lac}-hda-mCerulean. (**E**–**G**) Similar to Figure 3A–C but for a ΔDARS1 ΔDARS2 ΔdatA mutant with IPTG controllable expression of dnaA and mCerulean (P_{lac}-dnaA-mCerulean).*

bioRxiv preprint doi: https://doi.org/10.1101/2021.10.11.463968; this version posted October 11, 2021. The copyright holder for this preprint (which was not certified by peer review) is the author/funder, who has granted bioRxiv a license to display the preprint in perpetuity. It is made available under aCC-BY-NC-ND 4.0 International license.

Termination and initiation occur at similar cell sizes for intermediate growth rates

A striking feature of the fork plots in Figures 1–4 was that the branches do not show clear indications of overlapping rounds of replication. Instead, new branches started at about the same cell size as old branches ended. Assuming that the branches correspond to separate replication rounds, this implies that new rounds of replication are triggered in connection to the previous termination. In order to test if this is the case also for growth in other media than M9 succinate, we performed experiments in a number of different growth media to achieve different growth rates (Figure 5A; Figure S9). In Figure 5B, the data from all experiments in Figure 5A is plotted in the same coordinate system. The patterns remain when data from different growth conditions are pooled, suggesting that the spatial distribution of replication is mainly determined by cell size independently of growth rate.

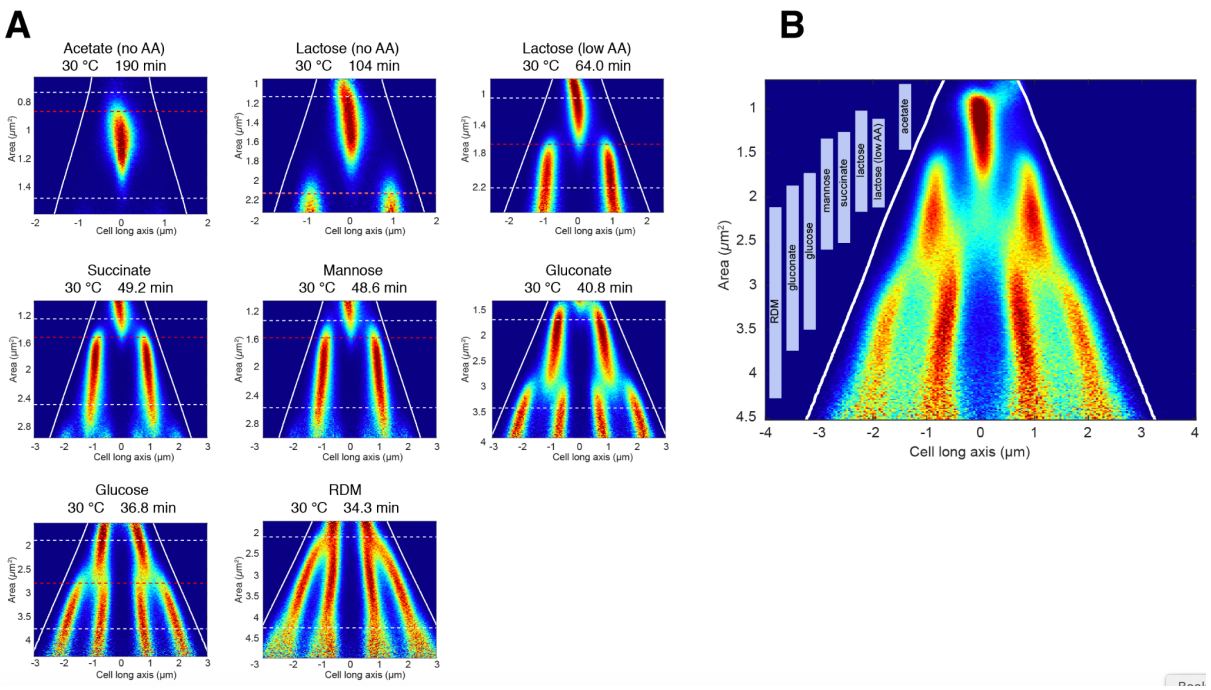

Figure 5. Replication patterns in different growth media. *(**A**) Fork plots for strains carrying YPet-DnaA grown in different media. Media, growth temperature and corresponding doubling time is given above each fork plot. (**B**) The same number of cells from the data in (A) pooled into one plot.*

As expected from the notion that branches correspond to separate rounds of DNA replication and that DNA content increases with growth rate (Dennis and Bremer, 1974), an increase in the growth rate resulted in an increase in the number of branches that appeared concurrently. For example, cells grown in M9 acetate had only one branch, cells grown in M9 succinate supplemented with amino acids had two branches occurring concurrently, and cells grown in M9 glucose supplemented with amino acids start four concurrent branches. More unexpectedly, the shape of the fork plots when branches disappear and reappear were similar for cases which initiate on two and on four chromosomes. It appeared that the pattern in cells that initiate on four chromosomes had just “doubled” the pattern from the cases which initiated on two chromosomes (Figure 5B). Seemingly, this would imply that also at fast growth rates with simultaneous replication of four chromosomes, new branches do not

bioRxiv preprint doi: https://doi.org/10.1101/2021.10.11.463968; this version posted October 11, 2021. The copyright holder for this preprint (which was not certified by peer review) is the author/funder, who has granted bioRxiv a license to display the preprint in perpetuity. It is made available under aCC-BY-NC-ND 4.0 International license.

start before the old ones have terminated. That is, we do not observe cells with six branches while going from two to four replicating chromosomes, which would be the clearest telltale phenotype of overlapping rounds of replication (Figure 5A; Figure S9). Instead, the fork plots for cells grown in glucose supplemented with amino acids and cells grown in RDM are similar in structure as the ones in slower growth (*e.g.* succinate), but with two primary differences: (i) the disappearance and appearance of the branches are less spatially separated, and (ii) in the RDM case, the initiation and termination events are appearing less well defined making the possibility of accurately determining initiation and termination virtually impossible from the fork plots.

Why do we expect overlapping rounds of replication when our fastest growth condition only supports growth at 34 min generation time? To provide stable imaging conditions, our experiments are typically performed at 30 °C. Based on the fact that the DNA replication time and the doubling time is expected to increase in a similar manner upon decreasing growth temperature (Bremer and Dennis, 2008), we expect growth conditions to be more important than temperature in terms of DNA replication overlap. To test this notion, we grew cells in M9 succinate supplemented with amino acids at 37 °C and found that the doubling time was 29.6 min and the corresponding fork plot (Figure S1B) does not show clear overlap between branches, further indicating that the replication time and doubling time scales similarly. Additional fork plots for cells grown in different media in 37 °C are found in Figure S9.

To get an independent measurement of the presence of overlapping DNA replication cycles, we performed a marker frequency analysis where we counted the abundance of each loci using Next Generation Sequencing. We fitted the decay of the coverage abundance from *oriC* to terminus with the function $b2^{-\frac{cx}{\tau}}$ (Bremer and Churchward, 1977), where τ is the doubling time and C is the duration of the C-period and x is a normalised genome location in which $x = 0$ at *oriC* and $x = 1$ at terminus (Figure 6). The results showed that the C-period and the doubling time have very similar lengths for cells grown at 30 °C in M9 succinate supplemented with amino acids, which is in line with the results shown in Figure 5A. There was a modest ~15% increase in C/τ ratio when the temperature was increased from 30 to 37 °C, which, in turn, is in line with the notion that the C-period and the doubling times scale similarly with temperature (Bremer and Dennis, 2008). However, for cells grown in glucose supplemented with amino acids, we found the C-period to doubling time ratio of ~1.3, suggesting overlapping replication which is contradicting our microscopy analysis (Figure 5A). The question of why the marker frequency and the microscopy analysis give different results is further investigated below.

In LB at 30 °C, our wt cells have a 36.5 min doubling time and the C-period to doubling time ratio is 1.8. Similar results were obtained using a qPCR-based approach of marker frequency analysis (Table S3). The marker frequency analysis for cells grown in succinate supplemented with amino acids at 30 °C supported the observation from the fork plots that termination and initiation occur at similar cell sizes. These size similarities exist for all conditions we observed with doubling times between 60 min and 40 min. We therefore investigated if termination is a contributor to triggering initiation under these conditions.

bioRxiv preprint doi: https://doi.org/10.1101/2021.10.11.463968; this version posted October 11, 2021. The copyright holder for this preprint (which was not certified by peer review) is the author/funder, who has granted bioRxiv a license to display the preprint in perpetuity. It is made available under aCC-BY-NC-ND 4.0 International license.

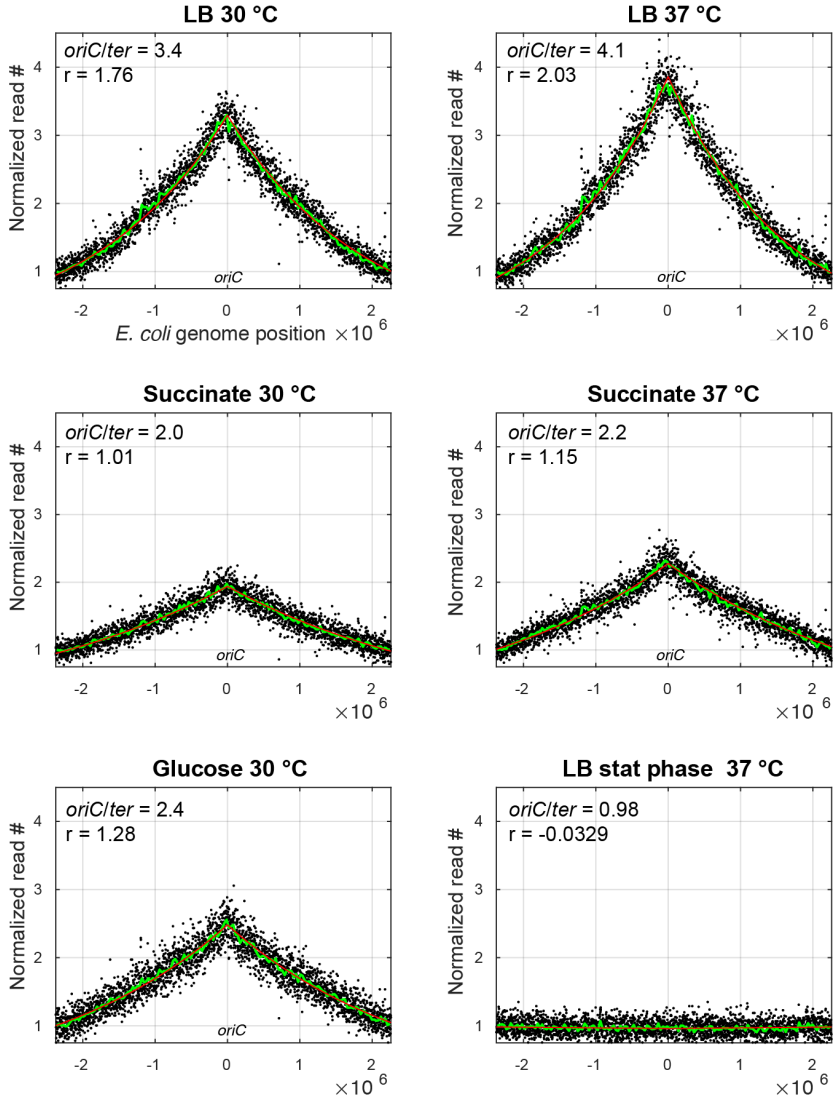

Figure 6. Marker frequency analysis. *Number of mapped reads (y-axis) for each chromosome region (x-axis) for different conditions (panel title) for a wt strain without any fluorescent labels. The genome coordinate is centered around oriC. The number of reads were binned into regions of either ~1.5 kb (black dots) or ~30 kb (green line) and normalised to the leftmost bin in each case. Red lines are the results of regression of the 30 kb binned data (green line) to the function* $y = B * 2^{(-C*x/\tau)}$*. Here, x is a normalised genome coordinate where* $x = 0$ *at oriC and* $x = 1$ *on the opposite side. Inset in each panel: oriC/ter ratio is calculated from regression as* $2^{(C/\tau)}$*.* $r = C\text{-period} / \text{generation time}$*. oriC/ter ratios based on qPCR with markers only in oriC and ter are shown in Table S3.*

bioRxiv preprint doi: https://doi.org/10.1101/2021.10.11.463968; this version posted October 11, 2021. The copyright holder for this preprint (which was not certified by peer review) is the author/funder, who has granted bioRxiv a license to display the preprint in perpetuity. It is made available under aCC-BY-NC-ND 4.0 International license.

Termination and initiation correlate in terms of cells size but not due to a direct mechanistic coupling

Could the lack of overlapping replication cycles at 40–60 min generation time be a sign that termination is triggering initiation via cessation of RIDA and the resulting reduction in DnaA-ATP to DnaA-ADP conversion? If so, we expect the sizes at termination and sizes at initiation to be correlated in single cells. To ensure meaningful termination to initiation size correlation, we first needed to make sure that beginnings and ends of time-lapse fluorescent foci trajectories were truly initiations and terminations. In Wallden et al. (Wallden et al., 2016), we showed that on average, a marker at the origin region spatially colocalizes with the replisome at initiation, implying that the appearance of a foci is truly initiation. In addition, we needed to verify if the terminus region was colocalized with the disappearance of the replisome track. To this end, we introduced a label on the terminus region via a *parS* sequence and a ParB-mCherry protein fusion. This allowed quantification of YPet-DnaN track endings while simultaneously estimating the distance to the *terminus* (Methods). The characterization of replisome branch endings was done in two growth conditions: Mannose supplemented with 1× RPMI amino acids and lactose supplemented with 0.025× RPMI. By making fork plots also for the terminus marker, we found that the terminus branch performs a rapid repositioning at a well-defined cell size, moving from the new pole to mid-cell (Figure 7A). The rapid repositioning is in line with previous observations of spatial position of the terminus loci (Lau et al. 2003). In mannose, the repositioning occured at similar cell sizes as initiation, while for cells grown in lactose supplemented with a low concentration of amino acids, the repositioning occured at a smaller size as compared to initiation. Importantly, in both cases, there was an overlap between terminus and replisome intensity density at the ends of the replisome branches. On the single-cell level, we found that the average distance between the replisome (YPet-DnaN) and terminus (*ter*-mCherry) is at a minimum when the YPet-DnaA trajectories ends, and that the distributions of replisome to terminus distances acquire a large peak of short distances close to YPet-DnaN track endings (Figure 7B). We concluded that the ends of the Ypet-DnaN trajectories are good indicators for termination and that the repositioning of the terminus is not a consequence of termination of DNA replication.

bioRxiv preprint doi: https://doi.org/10.1101/2021.10.11.463968; this version posted October 11, 2021. The copyright holder for this preprint (which was not certified by peer review) is the author/funder, who has granted bioRxiv a license to display the preprint in perpetuity. It is made available under aCC-BY-NC-ND 4.0 International license.

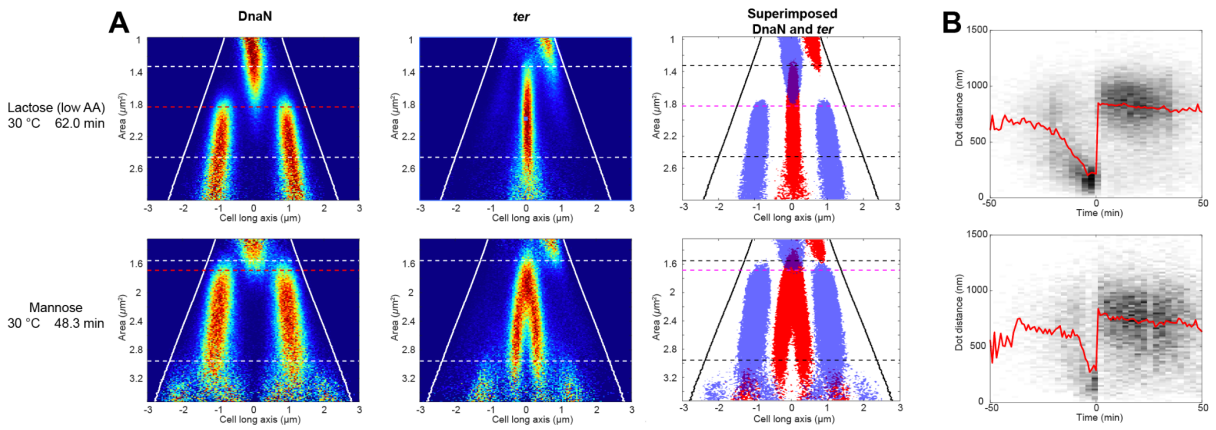

Figure 7. Distances between replisomes and termini in single cells. *(**A**) Fork plots of a strain that carries fluorescent markers for replication (a YPet-DnaN translational fusion; first column) and terminus (the ParB-mCherry/parS system, where parS is placed in the terminus region; second column). In the third column filled contours of the two fork plots have been superimposed. The lines are the same as in Figure 2A except white lines are now black and the red line is now in magenta. (**B**) Heat-map of 2D histograms for distances between YPet-DnaN and ParB-mCherry foci in single cells and relative time from YPet-DnaN track disappearance. Red lines indicate the median distance over time.*

Having substantiated the interpretation that single-cell YPet-DnaN trajectory beginnings and ends commonly correspond to initiation and termination of DNA replication, we correlated cell sizes at termination and initiation. For growth in succinate supplemented with amino acids, the division events and the termination/initiation events occured at similar sizes (Figure 5A). If the termination event would be captured right before division and initiation right after, this would generate highly unintuitive and hard to interpret correlation plots. To avoid the nuisance of division, we made use of “supercells" in which we followed a single lineage of descendants over multiple generations. The size at each event was then recorded as if division had not occurred (Figure 1B). Thus, in the first generation of descendents, initiation would occur at about twice the initiation size of the parent. In the second generation of descendants it would occur at about four times the size of the parent and so forth. We identified the beginnings and ends of the YPet-DnaN trajectories that we deemed reliable indicators of initiation and termination (see methods section for selection criteria). When we, for each supercell, plotted all detected initiation events on the *x*-axis and all detected termination events on the *y*-axis, this formed a number of different clusters (Figure 8B for cells grown in lactose supplemented with 0.025× amino acids; Figure S10 for all analysed conditions). The different clusters correspond to different combinations of events within the three generation lineage: clusters with a center of mass below the $y = x$ line are termination events together with the initiation events that, on average, occur subsequently in time. From these clusters, we estimated single-cell termination to initiation correlations (Figure 8C). Clusters where the termination event occurred at a cell size which was about twice as large as the cell size of the initiation event represents the initiation and end of the same round of replication. From these clusters, we estimated C-periods (Figure 8D) and growth rate correlations on the single-cell level (Figure 8E). The numerous other clusters are events separated by more than one generation. To avoid truncation bias, we made supercells consisting of three generations and only calculated correlation coefficients for events primarily occurring in the middle-most generation. We found that the correlation between the

bioRxiv preprint doi: https://doi.org/10.1101/2021.10.11.463968; this version posted October 11, 2021. The copyright holder for this preprint (which was not certified by peer review) is the author/funder, who has granted bioRxiv a license to display the preprint in perpetuity. It is made available under aCC-BY-NC-ND 4.0 International license.

size at termination and the size at the corresponding initiation was correlated with a Pearson correlation coefficient of ~0.4 (Figure 8C), tentatively suggesting that one round of replication termination triggers the next initiation.

However, for this correlation to be a real indicator of a mechanistic coupling between termination and initiation, it must decrease if the termination and initiation events are more separated in time. For cells grown in acetate, we know that replication only takes about half of the generation time (Wallden et al., 2016). To check for a decreasing trend in termination to initiation correlations, we imaged cells in three different conditions with decreasing growth rates as compared to succinate. However, we did not find the expected trend; the correlation coefficients stayed high also at slower growth (Figure 8C). We thus concluded that the correlation observed between size at termination and size of the corresponding initiation event is not in general due to a direct mechanistic coupling as would have been expected from turning off Hda mediated conversion of DnaA-ATP into DnaA-ADP.

bioRxiv preprint doi: https://doi.org/10.1101/2021.10.11.463968; this version posted October 11, 2021. The copyright holder for this preprint (which was not certified by peer review) is the author/funder, who has granted bioRxiv a license to display the preprint in perpetuity. It is made available under aCC-BY-NC-ND 4.0 International license.

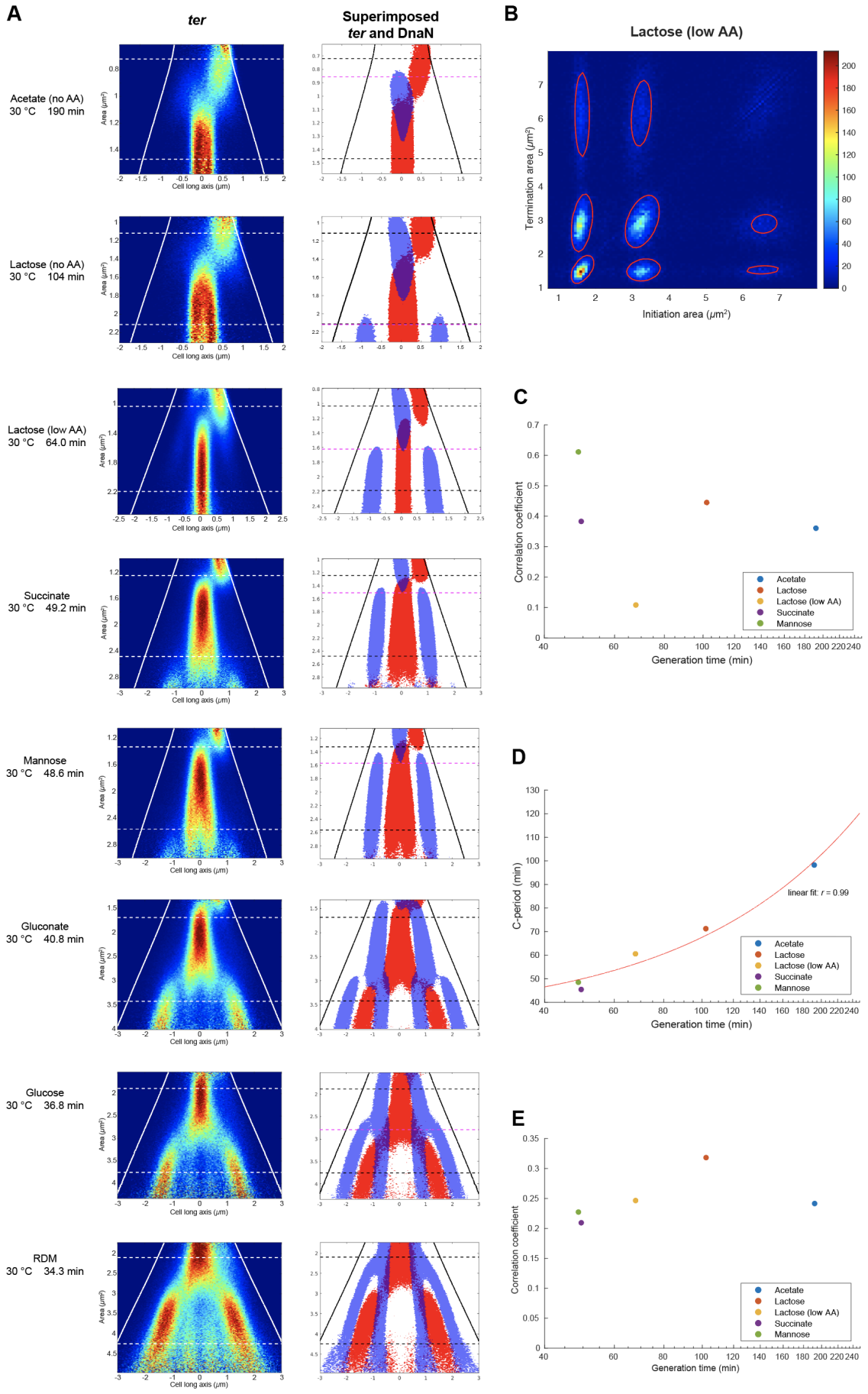

bioRxiv preprint doi: https://doi.org/10.1101/2021.10.11.463968; this version posted October 11, 2021. The copyright holder for this preprint (which was not certified by peer review) is the author/funder, who has granted bioRxiv a license to display the preprint in perpetuity. It is made available under aCC-BY-NC-ND 4.0 International license.

***Figure 8**. **Cell cycle parameters analysis in various growth conditions**. (**A**) Fork plots of a strain that simultaneously carry fluorescent markers for replication (a YPet-DnaN translational fusion; Figure 5A) and terminus (the ParB-mCherry/parS system, where parS is placed in the terminus region; first column). In the second column the results from YPet-DnaN (Figure 5A) have been superimposed onto the results from the terminus marker. The results are displayed as filled contours. Lines as in Figure 7B. (**B–E**) "Supercell" data (**B**) Example of a 2D histogram of the areas of all detected initiation and termination events for lineages of three generations, where the sizes of each event are defined as if the cells had not divided. Red lines show the result from clustering of the peaks in 2D histogram using a Gaussian Mixture Model (GMM).(**C**) Correlation between termination events and the next coming replication initiation event determined using GMMs as exemplified in (B) for five different growth media. (**D**) Correlation between average C-periods and average cell doubling times. (**E**) Correlation coefficients between single-cell C-periods within the same media and generation time sorted by the average generation time.*

Intensity based analysis shows no clear evidence of overlapping replication

We have already described how we observed overlapping rounds of DNA replication when using a marker frequency NGS-based method, but not when performing our standard fork plot microscopy analysis in M9 glucose supplemented with amino acids. Based on the results from the marker frequency analysis, we expected to see fork plots where the ongoing replication process continues after a new replication round has initiated as exemplified in Figure 9A. However, no such plot was observed for any growth condition (Figure 5A; Figure S9). It is, however, possible that the ongoing replication process continues after a new initiation has occurred, in the same spatial location as the newly initiated replication process. This is exemplified in the cartoon of Figure 9B. This replication fork dynamics would go undetected in our standard analysis of microscopy images, where only the detected coordinate of the foci enter the downstream analysis and figures. Thus, the analysis does not distinguish between single fluorescent replisomes, and foci which contain several copies of the replication machinery. Fluorescent foci that are made up of several replisomes will, however, be brighter.

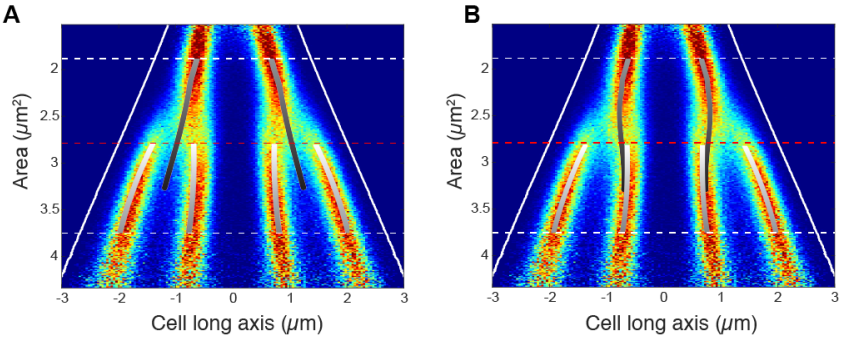

***Figure 9**. **Cartoons of overlapping replication in fork plots** (**A**) An imagined scenario where overlapping replication is seen as the two old branches continuing in between the four new branches, and (**B**), the overlapping replication seen as spatially coexistence of old and new replication forks within the inner most branches. The cartoons were constructed on top of a fork plot from cells grown in glucose medium. Doubling time 36.8 min.*

bioRxiv preprint doi: https://doi.org/10.1101/2021.10.11.463968; this version posted October 11, 2021. The copyright holder for this preprint (which was not certified by peer review) is the author/funder, who has granted bioRxiv a license to display the preprint in perpetuity. It is made available under aCC-BY-NC-ND 4.0 International license.

To overcome the problem of replisomes which are spatially colocalized, we generated fork plots based on the actual camera pixel intensities (Figure 10). We utilised the strain EL2990 with fluorescent markers both on the replisome and on the terminus. Here we expected the terminus marker and the replisome marker to be colocalized when replication terminates. The replisome label would indicate at what cell sizes that termination can occur. In the intensity-based fork plots, we expected parts of the fork plots to have transient periods of twice the fluorescence intensity in the regions with overlapping consecutive rounds. To capture the total intensity in each branch for all different area bins, the mid-cell intensity profile along the long axis of the cells were fitted to either a single, double or quadruple Gaussian function, depending on the number of peaks in the intensity profiles. In line with initiation and termination occurring at similar volumes, the growth in succinate showed no intensity peaks along the branches. In conflict with the marker frequency analysis, the inner branches in both RDM and M9 glucose showed no sign of regions with twice the fluorescence intensity. We note that given the continuous intensity increase in the outermost branches throughout the fork plot for RDM, we cannot assign a well-defined size at which initiation of DNA replication occurs for this condition. This wide cell-to-cell variability in initiation sizes would smear out the expected average intensity increase, possibly to such an extent that it is no longer possible to measure it. In the glucose case, on the other hand, the initiation size is well-defined, but the expected intensity increase following initiation is absent. This result is very hard to understand and the best interpretation we can come up with is that DnaN redistributes such that there is an approximately constant number of molecules associated with each replication focus. The mechanism for such redistribution is unknown.

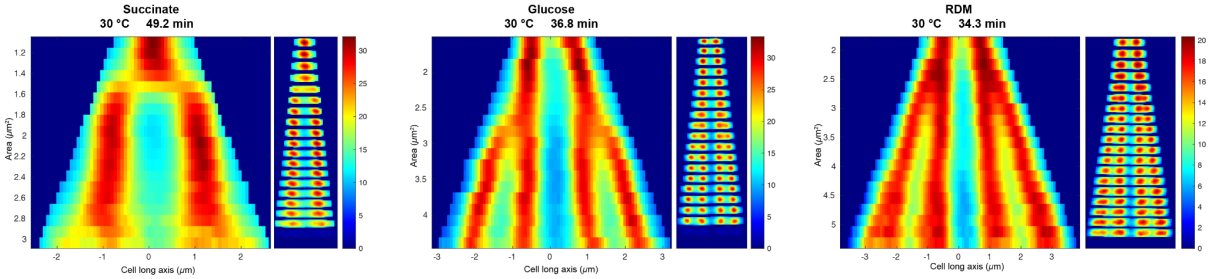

***Figure 10**. **Fork plots generated from camera pixel intensities.** To the right in each panel cells binned on sizes where the average YPet-DnaN intensities for each size bin are shown as heat maps. To the left in each panel a fork plot constructed for each size bin concatenating the middle-most lines of pixels along the long-axis of the average cell heat maps (to the right in each panel) are shown.*

Discussion

Our original intention in this project was to identify the mechanism for control of replication initiation in *E. coli* by mutating components known to be important for this process and characterizing the replication cycle in the resulting strains. It turned out that this strategy was useful to discard a number of previously suggested models:

Autoregulation of *dnaA* expression is not important for regulation of initiation since constitutive expression has only a minor impact on cell-to-cell variability in initiation size.

bioRxiv preprint doi: https://doi.org/10.1101/2021.10.11.463968; this version posted October 11, 2021. The copyright holder for this preprint (which was not certified by peer review) is the author/funder, who has granted bioRxiv a license to display the preprint in perpetuity. It is made available under aCC-BY-NC-ND 4.0 International license.

Initiator titration models based on DnaA expression are ruled out since individual lineages of cells can initiate in several consecutive generations after that DnaA synthesis is turned off.

Models based on regulating the balance of DnaA-ATP/ADP get some support from our data since cell-to-cell variability is strongly affected by *DARS1* deletion. However, the effect can be compensated by overexpression of DnaA or the removal of *datA*. This suggests that the role of *DARS1* is mainly to increase the DnaA-ATP level and that it is not critical for specific cell cycle regulation. Furthermore, any reasonable control system based on a DnaA-ATP/ADP switch should increase the initiation potential in proportion to the cell size or biomass and not in proportion to the number of a chromosomal site, such as *DARS*, since this would easily turn into an unstable positive feedback loop, *i.e.* more initiation leading to more DNA and thus more *DARS* sites that generate more DnaA-ATP that then causes more replication initiation*, etc*.

The most striking observation from mutating all known initiation regulators is that it is very hard to break the patterns that replication reinitiates at the same size as the previous round of replication seemingly has ended. This hints at a mechanical coupling of termination and the next initiation through inactivation of RIDA. It would however imply that the time it takes to replicate the chromosome (the C-period) needs to keep up with the generation time in all growth media and that there would be no overlapping replication cycles. In contrast, when we measure the ratios of origin and terminus using NGS we get the expected ratios corresponding to overlapping replication cycles. Thus, the NGS data rules out a mechanical coupling between termination and initiation, at least at fast growth rates. The coupling is also ruled out at slower growth rates as there is no correlation between the C-period and the growth rate at the single-cell level, and there is a correlation between termination and the subsequent initiation when termination and initiation are separated in time.

Despite the overlapping replication cycles, for example in glucose, the replication forks display well-separated branches. At the same time, we do not see a marked increase or decrease in the number of replication proteins per branch at any particular cell size. The only conclusion that remains is that replication is not triggered at a specific cell size under conditions where there are overlapping replication cycles and that the fixed initiation volume per origin only holds at average. At the same time, the well-determined spatial localization of the replication machinery is independent of the presence of overlapping replication cycles.

If we would try to make a simple conclusion from the rich sets of data analysed in this study, it would be that we have not found a simple mechanism that governs the coordination of replication and division cycles in *E. coli* at all growth rates. We have however shown that none of the previously described models are solely responsible for the regulation, at least not for all growth rates. It may be the case that there *is* no single mechanism that coordinates replication to cell growth at all growth rates, but that new systems have evolved progressively in *E. coli* to handle an increasingly broad range of growth conditions. For example, at slow growth, the accumulation of a sufficient number of DnaA to trigger replication at a fixed volume is enough; intermediate growth rates might require termination of RIDA at the end of the C-period coupled to DnaA-ATP conversion at *DARS*. At fast growth rates with overlapping replication cycles, SeqA mediated sequestration of the origin could have been introduced to prevent overinitiation when DnaA-ATP is abundant, possibly in combination with DiaA (Figure S4) as an additional positive regulator. Going forward, we

bioRxiv preprint doi: https://doi.org/10.1101/2021.10.11.463968; this version posted October 11, 2021. The copyright holder for this preprint (which was not certified by peer review) is the author/funder, who has granted bioRxiv a license to display the preprint in perpetuity. It is made available under aCC-BY-NC-ND 4.0 International license.

should consider that the mechanism may be more complex than we have appreciated so far, however unsatisfying this may seem.

Materials and Methods

Strains and media

The strain *E. coli* MG1655 BW25993 *phi80- rph+* (EL544) and derivatives thereof, were used in all experiments. The genotypes of all strains are listed in Table 1. If not stated otherwise, we have performed our experiments in M9 minimal media supplemented with 0.4% succinate and 1X RPMI 1640 amino acid solution (Sigma). All other media used are found in Table S1.

Table 1. *Strain list.*

Strain number	Strain	Genotype	Ref
EL544 (wt)	wt	*E. co* MG1655 BW25993 Δ*phi80 rph+*	This study
Derivatives of EL544			
EL421	*J23106-dnaA ΔdnaA*	Δ*galK ::J23106-dnaA ΔpdnaA-dnaA ::J23106-dnaA* (123 nt)	This study
EL838	*J23100-dnaA ΔdnaA*	Δ*galK ::J23100-dnaA ΔpdnaA-dnaA ::J23106-dnaA* (123 nt)	This study
EL787[a]	*J23101b-dnaA ΔdnaA*	Δ*galK ::J23101b-dnaA ΔpdnaA-dnaA ::J23106-dnaA* (123 nt)	This study
EL840	*J23106-dnaA ΔdnaA ΔDARS1*	Δ*galK ::J23106-dnaA ΔpdnaA-dnaA ::J23106-dnaA* (123 nt) Δ*DARS1*	This study
EL548	*J23106-dnaA ΔdnaA ΔDARS2*	Δ*galK ::J23106-dnaA ΔpdnaA-dnaA ::J23106-dnaA* (123 nt) Δ*DARS2*	This study
EL547	*J23106-dnaA ΔdnaA ΔdatA*	Δ*galK ::J23106-dnaA ΔpdnaA-dnaA ::J23106-dnaA* (123 nt) Δ*datA*	This study
EL562	*seqA-venus*	Δ*cobA ::seqA-venus-FRTcatFRT*	This study
EL2470	*seqA-venus ΔDARS1*	Δ*cobA::seqA-venus-FRTcatFRT ΔDARS1*	This study
EL2095	*seqA-venus ΔDARS2*	Δ*cobA::seqA-venus-FRTcatFRT ΔDARS2*	This study
EL2097	*seqA-venus ΔdatA*	Δ*cobA::seqA-venus-FRTcatFRT ΔdatA*	This study
EL2297	*seqA-venus ΔDARS1 ΔDARS2 ΔdatA*	Δ*cobA::seqA-venus-FRTcatFRT ΔDARS1 ΔDARS2 ΔdatA*	This study
EL862	*seqA-venus J23100-dnaA ΔdnaA*	Δ*cobA ::seqA-venus-FRTcatFRT* Δ*galK ::J23100-dnaA ΔpdnaA-dnaA ::J23106-dnaA* (123 nt)	This study
EL2660	*seqA-venus J23100-dnaA ΔdnaA ΔDARS1*	Δ*cobA ::seqA-venus-FRTcatFRT* Δ*galK ::J23100-dnaA ΔpdnaA-dnaA ::J23106-dnaA* (123 nt) ΔDARS1	This study
EL868[a]	*seqA-venus J23101b-dnaA ΔdnaA*	Δ*cobA ::seqA-venus-FRTcatFRT* Δ*galK ::J23101b-dnaA ΔpdnaA-dnaA ::J23106-dnaA* (123 nt)	This study
EL558	*seqA-venus J23106-dnaA ΔdnaA*	Δ*cobA ::seqA-venus-FRTcatFRT* Δ*galK ::J23106-dnaA ΔpdnaA-dnaA ::J23106-dnaA* (123 nt)	This study
EL864	*seqA-venus J23106-dnaA ΔdnaA ΔDARS1*	Δ*cobA ::seqA-venus-FRTcatFRT* Δ*galK ::J23106-dnaA ΔpdnaA-dnaA ::J23106-dnaA* (123 nt) Δ*DARS1*	This study
EL586	*seqA-venus J23106-dnaA ΔdnaA ΔDARS2*	Δ*cobA ::seqA-venus-FRTcatFRT* Δ*galK ::J23106-dnaA ΔpdnaA-dnaA ::J23106-dnaA* (123 nt) Δ*DARS2*	This study
EL560	*seqA-venus J23106-dnaA ΔdnaA ΔdatA*	Δ*cobA ::seqA-venus-FRTcatFRT* Δ*galK ::J23106-dnaA ΔpdnaA-dnaA ::J23106-dnaA* (123 nt) Δ*datA*	This study
EL771	*seqA-venus J23106-dnaA ΔdnaA ΔDARS1 ΔDARS2*	Δ*cobA ::seqA-venus-FRTcatFRT* Δ*galK ::J23106-dnaA ΔpdnaA-dnaA ::J23106-dnaA* (123 nt) Δ*DARS1 ΔDARS2*	This study
EL929	*seqA-venus J23106-dnaA ΔdnaA ΔDARS1 ΔdatA*	Δ*cobA ::seqA-venus-FRTcatFRT* Δ*galK ::J23106-dnaA ΔpdnaA-dnaA ::J23106-dnaA* (123 nt) Δ*DARS1 ΔdatA*	This study
EL502	*seqA-venus J23106-dnaA ΔdnaA ΔDARS2 ΔdatA*	Δ*cobA ::seqA-venus-FRTcatFRT* Δ*galK ::J23106-dnaA ΔpdnaA-dnaA ::J23106-dnaA* (123 nt) Δ*DARS2 ΔdatA*	This study
EL500	*seqA-venus J23106-dnaA ΔdnaA ΔDARS1 ΔDARS2 ΔdatA*	Δ*cobA ::seqA-venus-FRTcatFRT* Δ*galK ::J23106-dnaA ΔpdnaA-dnaA ::J23106-dnaA* (123 nt) Δ*DARS1 ΔDARS2 ΔdatA*	This study
EL931	*seqA-venus J23106-dnaA ΔdnaA ΔdiaA*	Δ*cobA ::seqA-venus-FRTcatFRT* Δ*galK ::J23106-dnaA ΔpdnaA-dnaA ::J23106-dnaA* (123 nt) Δ*diaA*	This study
EL2128	*seqA-venus J23106-dnaA ΔdnaA ΔDARS2 ΔdatA ΔdiaA*	Δ*cobA ::seqA-venus-FRTcatFRT* Δ*galK ::J23106-dnaA ΔpdnaA-dnaA ::J23106-dnaA* (123 nt) Δ*DARS2 ΔdatA ΔdiaA*	This study
EL1548	*seqA-venus plac-dnaA-mcerulean ΔdnaA*	Δ*cobA ::seqA-venus-FRTcatFRT* Δ*lacZYA ::dnaA-mcerulean3-FRT ΔpdnaA-dnaA ::J23106-dnaA* (123 nt)	This study
EL2822	*seqA-venus plac-dnaA-mcerulean ΔdnaA ΔDARS1 ΔDARS2 ΔdatA*	Δ*cobA ::seqA-venus-FRTcatFRT* Δ*lacZYA ::dnaA-mcerulean3-FRT-kanR-FRT ΔpdnaA-dnaA ::J23106-dnaA* (123 nt) Δ*DARS1 ΔDARS2 ΔdatA*	This study
EL2736	*seqA-venus plac-hda-mcerulean*	Δ*cobA ::seqA-venus-FRTcatFRT* Δ*lacZYA ::hda-mcerulean3-FRT-kanR-FRT*	This study
EL2931	*seqA-venus ΔydbL ::parS ΔgtrA ::mCherry-parB*	Δ*cobA ::seqA-venus-FRTcatFRT ΔydbL ::parS-FRT-cat-FRT ΔgtrA ::p58-mCherry-parB-SpR*	This study
EL2990	*ypet-dnaN ΔydbL ::parS ΔgtrA ::mCherry-parB*	*kan-ypet-dnaN ΔydbL ::parS-FRT-cat-FRT ΔgtrA ::p58-mCherry-parB-SpR*	This study
EL2938	*dnaQ-ypet ΔydbL ::parS ΔgtrA ::mCherry-parB*	*dnaQ-yfp-FRT-kanR-FRT ΔydbL ::parS-FRT-cat-FRT ΔgtrA ::p58-mCherry-parB-SpR*	This study

[a]The J23101b promoter is based on J23101 but carries one missmatch (TTTACAGCTAGCTCAGTCCTAGGTATAATGCTAGC instead of TTTACAGCTAGCTCAGTCCTAGGTATTATGCTAGC

Chromosomal modifications

For construction of chromosomal mutations (deletions, fusions, replacements) λ Red recombineering (Datsenko and Wanner, 2000; Yu et al., 2000) was used. The λ Red genes were expressed from plasmid pSIM5-Tet (Koskiniemi et al., 2011). As selectable/counter selectable markers we used *Acatsac1* (GenBank acc. # MF124798.1) or *Akansac1*, carrying a *cat* gene (conferring chloramphenicol resistance) or *kan* gene (conferring kanamycin resistance) for positive selection, and the *B. subtilis sacB* gene (conferring sensitivity to sucrose) for negative selection. Generalized transduction using phage P1 *vir (Thomason et al., 2007)* was used for transferring mutations between strains. For many experiments, the

bioRxiv preprint doi: https://doi.org/10.1101/2021.10.11.463968; this version posted October 11, 2021. The copyright holder for this preprint (which was not certified by peer review) is the author/funder, who has granted bioRxiv a license to display the preprint in perpetuity. It is made available under aCC-BY-NC-ND 4.0 International license.

chromosomal construct *cobA*::*seqA-venus* was introduced in the strains keeping the native *seqA* gene intact. In contrast to having *seqA-venus* as the only source of SeqA in the strains, this mutant had no effect on exponential growth.

The chromosomal knockouts of replication regulators (*DARS1*, *DARS2*, and *datA*) are all marker free and scar free and were made using two different methods: (i) through single strand λ Red where we cured an inserted selectable/counterselectable marker by an oligo covering the junction of the desired deletion. (ii) through the DIRex method (Näsvall, 2017). Mutations were transferred between strains through generalized transduction with phage P1.

IPTG inducible DnaA. Two overlapping DNA fragments were simultaneously transformed through electroporation into a strain that expressed the λ Red genes. One fragment was synthesized and contained bp 150–390 of the *lacZ* gene followed by stop codons in all frames, and the *dnaA* gene (including its ribosome binding site) transcriptionally fused to *mCerulean* MP. The other was a PCR fragment containing 40 bp homology to the first fragment, a *kan* gene flanked on both sides by Flp recombinase target (FRT) sites, and 40 bp homology to the sequence downstream of the *lacA* gene. The resulting recombinants thus had everything between bp 390 in *lacZ* until just after the *lacA* gene replaced by *dnaA-mCerulean-FRT-kan-FRT*, leaving *dnaA* transcriptionally fused to the beginning of the *lacZ* gene. This construct was transduced to our *seqA-venus* strain and thereafter *kan* was removed by expression of Flp recombinase from plasmid pCP20 (Cherepanov and Wackernagel, 1995) , leaving a scar containing a single FRT site. Finally, the native *dnaA* gene was replaced by the J23106 promoter as described above. The resultant strain, EL1548, is hence dependent on IPTG induction of P_{lac}-*dnaA* for growth.

IPTG inducible Hda. First *dnaA* in P_{lac}-*dnaA-mCerulean* (see above) was replaced by an *Acatsac1* cassette. The resulting strain was transformed with a PCR fragment containing the *hda* gene and its ribosome binding site, resulting in P_{lac}-*hda-mCerulean*. The native *hda* gene was kept intact.

Constitutively expressed DnaA mutants. Firstly, we exchanged an *Acatsac1* cassette in the selectively neutral *galK* locus by PCR-fragments containing J23100-*dnaA*, J23101b-*dnaA*, and J23106-*dnaA*, selecting sucrose resistant recombinants. Next, the native *dnaA* gene was deleted by replacing it by *Acatsac1*, whereafter *Acatsac1* in turn was replaced by an oligo containing the J23106 promoter (to allow constitutive expression of the rest of the operon). Similar to the IPTG inducible DnaA strain, 123 nt were kept in the end of *dnaA*.

parS/parB. This system was adapted from (Nielsen et al., 2006) and was recently modified in (Wiktor et al., 2021). Here, we transformed *parS* into a neutral position in the terminus region by exchanging y*dbL* for *parS*-FRT-*cat*-FRT. *mCherry-ParBMt1* (Δ*gtrA*::*p58-mCherry-parB-SpR*; (Wiktor et al., 2021)) was introduced through P1 transduction.

Other chromosomal constructs originated from other labs and were P1 transduced into our strains (*kanR-ypet-dnaN* and *dnaQ-ypet*-FRT-*kanR*-FRT (Reyes-Lamothe et al., 2010), or introduced in another chromosomal location through λ Red *seqA-venus*-FRT-*cat*-FRT (Babic et al., 2008).

bioRxiv preprint doi: https://doi.org/10.1101/2021.10.11.463968; this version posted October 11, 2021. The copyright holder for this preprint (which was not certified by peer review) is the author/funder, who has granted bioRxiv a license to display the preprint in perpetuity. It is made available under aCC-BY-NC-ND 4.0 International license.

Proteomic analysis

The proteomic analyses were performed as described in (Knöppel et al., 2020). Briefly, cultures were started by inoculating 50 ml succinate medium with 250 µl overnight culture. The cultures were allowed to grow to OD_{600} = 0.2, pelleted by centrifugation and washed twice in PBS. The pellets were frozen before further preparation. In the medium switch experiment, two flasks with 10 ml succinate medium with 1 mM IPTG were inoculated with 250 µl overnight culture and the cultures were grown for 3 h, after which they were pelleted by centrifugation and washed twice with succinate medium (without IPTG). The pellets were resuspended in 50 ml pre-warmed succinate medium and allowed to continue growing for 90 or 180 minutes before being pelleted, washed twice in PBS and frozen. The proteomics core facility at the Sahlgrenska Academy, Gothenburg University, homogenized the samples, digested with trypsin and labeled the peptides with TMT 10-plex isobaric tagging reagents, and performed relative quantification of peptides by LC-MS/MS, as described in (Knöppel et al., 2020).

Microscopy

Optical configurations

Six different optical configurations were used. Each configuration is listed and given a name below, including references to which configuration was used to generate which figure/panel.

Configuration 1: The microscope was an inverted TiE (Nikon) microscope with a CFI Plan Apo lambda 1.45/100x oil objective (Nikon). Phase contrast images were acquired on a DMK 38UX30 (The Imaging Source) camera. Bright-field and fluorescence images were acquired on a iXon Ultra 888 (Andor) camera. TLED+ (Sutter Instruments) with a white LED was used as a light source for phase contrast and bright-field images. For fluorescence images the cells were episcopically illuminated by a 5.3 W/cm^2 light beam from a 514 nm Genesis CX-STM 2000 mW (Coherent) laser and when applicable from a 445 nm 06-MLD 120 mW (Cobolt) laser. The power used with the 445 nm laser as indicated in each separate experiment. The 514 nm laser light was reflected onto the sample using the dichroic mirror Di02-R514 (Semrock) and the emitted fluorescence passed the same dichroic and was filtered through a BrightLine FF01-474/27 (Semrock) emission filter. The 445 nm laser light was reflected onto the sample using the dichroic mirror Di02-R442 (Semrock) and the emitted fluorescence passed the same dichroic and was filtered through a BrightLine FF01-550/49 (Semrock) emission filter. This configuration was used in Figure 2A ($P_{J23101b}$-*dnaA*), Figure 2B, Figure 4B (P_{J23106}-*dnaA ΔDARS2;* P_{J23106}-*dnaA ΔDARS1 ΔDARS2 ΔdatA*), Figure 4C (P_{wt}-*dnaA ΔDARS2;* P_{wt}-*dnaA ΔdatA;* P_{wt}-*dnaA ΔDARS1 ΔDARS2 ΔdatA*), Figure S3, Figure S4 and Figure S5. The supplemental figures contain the same genotypes as in Figure 2A and Figures 4B–C, respectively, and internal references for which experiment which either were the P_{wt}-*dnaA* or P_{J23106}-*dnaA* strains.

Configuration 2: Similar to Configuration 1 but with the differences being that a red 630 nm LED (Sutter Instruments) was used for phase contrast, a 600 nm short-pass filter (Edmund Optics) was placed in the microscope camera port for the iXon Ultra, the laser lights were mirrored on FF468/526/596-Di01 (Semrock), and the emitted fluorescence was filtered through a FF01-484/543/702 BrightLine (Semrock) emission filter. This configuration was

bioRxiv preprint doi: https://doi.org/10.1101/2021.10.11.463968; this version posted October 11, 2021. The copyright holder for this preprint (which was not certified by peer review) is the author/funder, who has granted bioRxiv a license to display the preprint in perpetuity. It is made available under aCC-BY-NC-ND 4.0 International license.

used in Figure 4B (P_{J23106}-*dnaA ΔDARS1 ΔdatA*), Figure 4C (P_{tr}-*dnaA ΔDARS1*), Figure 4D (*hda* P_{lac}-*hda-mCerulean*), Figure S4, Figure S5 and Figure S9 (only the experiment with RDM). The supplemental Figures S4 and S5 show the same genotypes as in Figure 4B–C respectively and the internal references run in the same experiment. The references were either the P_{wt}-*dnaA* or P_{J23106}-*dnaA* strains.

Configuration 3: Similar to Configuration 1 except the laser was a 515 nm 06-MLD (Cobolt). This configuration was used in Figure 2A (P_{wt}-*dnaA*; P_{J23106}-*dnaA*), Figure 4B (P_{J23106}-*dnaA ΔDARS1;* P_{J23106}-*dnaA ΔdatA;* P_{J21306}-*dnaA ΔDARS1 ΔDARS2;* P_{J23106}-*dnaA ΔDARS2 ΔdatA*), Figure S1B (YPet-DnaN 37 °C), Figure S3, Figure S4 and Figure S5. The supplemental Figures S3, S4 and S5 show the same genotypes as in Figure 2A and Figures 4B–C respectively and the internal references run in the same experiment. The references were either the P_{wt}-*dnaA* or P_{J23106}-*dnaA* strains.

Configuration 4: Similar to Configuration 1 but the lasers used for fluorescence imaging were 515 nm (Fandango 150, Cobolt) and 580 nm (VFL, MBP Communications). The laser power was set to 5 W/cm^2 for both lasers. Fluorescence images were acquired using a Kinetix sCMOS (Teledyne Photometrics) camera. The laser lights were reflected onto the sample using a FF444/521/608-Di01 (Semrock) triple-band dichroic mirror and the emitted fluorescence passed through the same dichroic mirror. The emitted fluorescence was also passed through a BrightLine FF580-FDi02-T3 (Semrock) dichroic beamsplitter. The split fluorescence was then filtered through BrightLine FF01-505/119-25 (Semrock) and BrightLine FF02-641/75-25 (Semrock) filters. The fluorescence was focused on two different parts of the camera chip. Phase contrast images were acquired using a DMK 38UX304 (The Imaging Source) camera. A TLED+ (Sutter Instruments) with a 480 nm LED was used as a light source for acquisition of phase contrast images. The transmitted light was passed through a FF444/521/608-Di01 (Semrock) triple-band dichroic mirror and reflected onto the camera using a Di02-R514 (Semrock) dichroic mirror. This configuration was used in Figure 7.

Configuration 5: The configuration was the same as in (Camsund et al., 2020). This configuration was used in Figure S9 (all fork plots except RDM).

Configuration 6: The configuration was the same as in (Wiktor et al., 2021). This configuration was used in Figure 1, Figure 3, Figure 4E–G, Figure 5, Figure 8, Figure 10, Figure S1A, Figure S1B (YPet-DnaN 30 °C), Figure S8, and Figure S10.

Cell preparation

The day before each experiment two strains (a reference and a strain of interest) were inoculated into separate tubes from frozen stock cultures stored at -80 °C. The tubes contained the intended media of the experiment. Cells were grown overnight in a 30 or 37 °C shaking incubator (200 rpm) depending on which temperature the experiment was performed in. On the day of the experiment, cells were diluted either 1:250 or 1:1000 in fresh media and grown for 2–4 h before loading on the microfluidic device or cells were loaded from stationary phase into the microfluidic device. Cells were allowed to grow for 6–9 h before starting the experiment if loaded directly from stationary phase and 2–7 h if the culture was diluted. For the experiment performed in M9 acetate, cells were first inoculated from -80 °C into LB and grown overnight at 37 °C in a 200 rpm shaking incubator. The next

bioRxiv preprint doi: https://doi.org/10.1101/2021.10.11.463968; this version posted October 11, 2021. The copyright holder for this preprint (which was not certified by peer review) is the author/funder, who has granted bioRxiv a license to display the preprint in perpetuity. It is made available under aCC-BY-NC-ND 4.0 International license.

day cells were diluted 1:100 into fresh M9 acetate media and grown for roughly 24 h before being loaded onto the chip. The cells were then allowed to grow for roughly 24 hours before image acquisition was started. In the DnaN-terminus distance experiment (Figure 7) only one strain was used. For the experiments performed with strains EL1548 and EL2822 the media was supplemented with the starting concentration of IPTG.

Microfluidic experiments

Experiments were performed using a PDMS mother-machine type device with open ended channels that also allow for loading of two separate strains (Baltekin et al., 2017). To keep media flowing, pressure on the different ports were maintained with OB1 MK3+ microfluidic flow controller (Elveflow). This controller was also used to load cells. The microfluidic devices used had four different sizes on the traps (875, 1000, 1125 and 1250 nm). The 875 nm sized devices were used for the experiments with M9 acetate and M9 lactose (Figure 5, Figure 8 and Figure S10). The 1000 nm sized devices were used for the M9 lactose 0.025x RPMI (Figure 5, Figure 7, Figure 8 and Figure S10), M9 mannose 1x RPMI (Figure 5, Figure 7, Figure 8 and Figure S10) and M9 succinate 1x RPMI ± IPTG (Figure 1, Figure 2, Figure 4, Figure 5, Figure 9, Figure 10, Figure S1, Figure S3–S5, Figure S8 and Figure S10) experiments except for the experiment in Figure 3 which used a 1125 nm sized device. The 1125 nm sized devices were used for the M9 gluconate experiment (Figure 5, Figure 8 and Figure S10). The 1250 nm sized devices were used for the M9 glucose 1x RPMI experiments (Figure 5, Figure 8 and Figure 10) and RDM experiments (Figure 5, Figure 8, Figure 10 and Figure S9). In Figure S9 all experiments except RDM were run in 1000 nm sized devices.

In the experiments with DnaA-ATP/ADP regulatory mutants (Figures 4B–C) and mutants with constitutively expressed DnaA (Figure 2A) experiments were run for 12–16 h where phase contrast images were acquired every 30 s with an exposure time of 100 ms while fluorescence images were acquired every 2 min with an exposure time of 300 ms. For the experiments run on Configurations 1 and 3, bright-field images were acquired every 2 min with an exposure time of 100 ms. For the experiments performed on Configuration 2 a bright-field and a corresponding phase contrast image were acquired before experiments were started. Bright-field images were used for landmark based registration.

In the experiment with five different concentrations of IPTG (50, 75, 100, 125 and 150 μM; Figure 2B), the experiment was divided into six different parts where each part corresponds to a specific IPTG concentration. In parts one through five (50–150 μM IPTG), cells were imaged for 6 h at each IPTG concentration. A roughly 15 min break in image acquisition was done before the switch between 125 and 150 μM IPTG was performed. In the sixth part, the media was switched back to 50 μM IPTG and imaging continued for another 10 h. To switch between the five different media an M-switch and a 2-Switch from Fluigent was used. Replication was monitored by imaging a set of cells in phase contrast every 1 min (100 ms exposure time) while bright-field (100 ms exposure time) and 514 nm fluorescence images were acquired every 2 min (300 ms exposure time). For a different set of cells, the change in mCerulean fluorescence intensity was monitored. Phase contrast (100 ms exposure time), bright-field (100 ms exposure time) and 445 nm fluorescence images (300 ms exposure time) were acquired every 16 min. The power of the laser was set to 2.97 W/cm^2.

bioRxiv preprint doi: https://doi.org/10.1101/2021.10.11.463968; this version posted October 11, 2021. The copyright holder for this preprint (which was not certified by peer review) is the author/funder, who has granted bioRxiv a license to display the preprint in perpetuity. It is made available under aCC-BY-NC-ND 4.0 International license.

The two experiments with strains EL1548 and EL2822 were run over the course of 5.5–6 h. Here cells were imaged for 90 min while the media contained 1 mM IPTG. Image acquisition was then stopped to manually change the tubing for ports that supplied media over the cells. The tubing that was supplying media over the channels behind the constrictions were swapped out first. The tubing that supplied media that was flown over the cells was exchanged afterwards. While switching out tubes, media containing IPTG was continuously flown over the cells from another tube. Image acquisition restarted 16–23 min after the first round of imaging finished. Cells were imaged 4 h after the switch. Throughout the experiment a set of cells were imaged every 1 min with phase contrast (50 ms exposure time) and every 2 min with the TEAL setting (300 ms exposure time) on the Spectra Gen 3 (Lumencor) light source. Additionally, to approximate the amount of DnaA cells were imaged every 10 min in phase contrast (130 ms exposure time) and fluorescence with the BLUE setting (100 ms exposure time) to excite the transcriptionally fused mCerulean. Here a new set of cells were imaged each time to avoid any effect of photobleaching.

In the *hda-overexpression* experiment (Figure 4D) three different imaging regimes were set up over the duration of the experiment (7 h). The regimes were from hour 0–2, 2–3, and 3–7. In the first regime a set of cells were imaged in phase contrast and with the 445 nm laser every 10 min (100 ms and 1 s exposure time respectively). Here, the same set of cells were only imaged once in the 2 h interval. After 2 h, the medium was switched to medium with 1 mM IPTG using the previously mentioned flow controller. In the second regime images were acquired similarly to the first regime except new cells were imaged every 2 min. For the last regime imaging was done the same as in regime one. Here, the same set of cells were imaged as well and they were imaged twice during the duration of this regime. Lastly, during the whole experiment a different set of cells were imaged in phase contrast every 30 s (100 ms exposure time) and with the 514 nm laser every 2 min (300 ms). The power of the 445 nm laser was set to 4.97 W/cm^2. mCerulean fluorescence data not shown.

In experiments performed on Configuration 4 (Figure 7) imaging was performed for 10 h. Phase contrast images were acquired every 1 min (50 ms exposure time). Fluorescence images were also acquired every 1 min (150 ms exposure time), with each acquisition triggering both 515 nm and 580 nm lasers back-to-back by the camera through function generators (Tektronix), one for each laser. The power of both lasers was set to 5 W/cm^2.

In the experiments performed on Configuration 5 (Figure S9, all fork plots except the RDM one) image acquisition lasted for 8 h. In these experiments two different media were run on each side of the chip. Phase contrast images were acquired every 1 min (20 ms exposure time) and 514 nm fluorescence images every 2 min (300 ms exposure time) with a power of 5.3 W/cm^2.

The experiments performed with different carbon sources on Configuration 6 (Figure 1, Figure 5, Figure 8, Figure 10, Figures S1A and S1B[1], and Figure S10) were all run for 12 h except for the ones run with acetate and RDM, which were run for 24 and 9 h respectively. Similarly, phase contrast images were acquired every 30 s (50 ms exposure time) and fluorescence images every 2 min with 300 ms exposure time for both colors (YPet-DnaN were excited using the TEAL setting while ParB-mCherry was excited by the YELLOW setting on the Spectra Gen 3 (Lumencor) light source). However, in the acetate experiment

[1] Only the YPet-DnaN 30 °C experiment.

bioRxiv preprint doi: https://doi.org/10.1101/2021.10.11.463968; this version posted October 11, 2021. The copyright holder for this preprint (which was not certified by peer review) is the author/funder, who has granted bioRxiv a license to display the preprint in perpetuity. It is made available under aCC-BY-NC-ND 4.0 International license.

phase contrast images were acquired every 2 min and fluorescence images every 8 min and for the RDM experiment phase contrast images were acquired every 20 s and fluorescence images every 80 s. The settings were otherwise the same as for the other media.

Image analysis

Image analysis pipeline

A fully automated image analysis pipeline previously described (Camsund et al., 2020; Wiktor et al., 2021) primarily written in MATLAB (Mathworks) was used. However, different segmentation algorithms were used depending on which microscope configuration that was used. For Configuration 1, 2, 3, and 5 segmentation was performed using per object ellipse fit (Ranefall et al., 2016). For Configuration 4 and 6 a nested Unet neural network (Ronneberger et al., 2015) was used. Additionally, in Configuration 1, 2, 3, and 4 landmark based registration was performed between the two cameras. This was not done on Configuration 5. On Configuration 6 landmark based registration was performed in the replisome-*terminus* experiments between the two different emission filters. To do this images of 500 nm fluorescent beads (TetraSpeck, Thermo Fisher) were imaged in both channels.

Post-processing

Custom written MATLAB 2020b (Mathworks) functions and scripts were used for processing the pipeline output. For estimation of single-cell initiation and termination areas detected foci of either SeqA-Venus or YPet-DnaN were linked together and tracked using the u-track algorithm (Jaqaman et al., 2008). The parameters were optimized to be able to identify starts of tracks by allowing for merging and splitting. To avoid truncation issues when tracking dots, cell lineages consisting of either three, four or five generations were created. Furthermore, these generations were concatenated into a “supercell” where the area $A(t)$ at a given time point t is given by $A(t) = A(last) + 2^i(a^c(t) - d_{frac}a^p(last))$, where $A(last)$ is the area of the supercell before division, i is an index for the generation in the lineage, a^c are the areas of the cell in generation i, d_{frac} is the area fraction of the two sisters right after division and $a^p(last)$ is the area right before division in generation $i-1$. With this initiation events were defined as the start of a trajectory that was longer than 11 frames fluorescence frames (all experiments when applied except for the experiment in M9 acetate where trajectories had to be at least 9 frames long), it did not start on the first two frames of a supercell and the two adjacent frames had to have good segmentation (no gap in cell-tracking, sufficiently high Jaccard index and no convergence between cells). Termination events were defined as the end of tracks with the same criteria for initiation and some further criteria as well. Those criteria were that tracks could not end in the last two frames of supercells, tracks had to be spatially located within the boundary of the daughter used to build the supercell or in cases where initiation occurred close to division the long-axis coordinate of the last frame of a trajectory could maximally move 5 pixels from the current generation’s mid-cell. Supercells were then filtered to require at least one initiation and termination event as well as containing unique individual cells. The main cell by which each supercell was identified had to itself be detected for at least 20 phase contrast frames, it had to have a parent, a sister and daughters living for at least 10 phase contrast frames.

bioRxiv preprint doi: https://doi.org/10.1101/2021.10.11.463968; this version posted October 11, 2021. The copyright holder for this preprint (which was not certified by peer review) is the author/funder, who has granted bioRxiv a license to display the preprint in perpetuity. It is made available under aCC-BY-NC-ND 4.0 International license.

Average initiation areas and coefficient of variations (CV) as displayed in Figure 2A, Figures 4B–D, Figure 5, Figure 8, Figure S3, Figure S4 and Figure S5 were determined by using MATLAB's fit('gauss') function equal to the number of generations used to generate supercells. Numbers were either taken from what corresponds to the second or third generation to avoid truncation bias. In Figure 1A medians were calculated as the median from each generation's distribution of initiation areas. In Figure 2B, Figures 3A and 3B, Figures 4E and 4F, Figure 7, Figure S1. Figure S8 and Figure S9 average initiation areas were determined as in (Camsund et al., 2020)'s estimation of average initiation sizes in bulk.

Correlations between termination and the subsequent initiation event were determined by matching all initiation and termination events in each supercell. These matched events formed clusters in a 3-by-3 grid (in total 9 clusters). Clusters where the line $y = x$ intersects correspond to events occurring in the same generation, clusters below this line correspond to initiation events occurring after termination events and clusters above this line correspond to termination events occurring after initiation events. Matched events that were much larger than what the clusters corresponding to the third generation were removed before the clusters were classified with a Gaussian mixture model. In all conditions except M9 acetate an extra cluster to deal with background was used. Then posterior probabilities were calculated for each matched event and events with a lower probability than 0.9 were discarded. Correlation coefficients were calculated for each cluster and the clusters corresponding to initiation and termination occurring in the second generation were chosen for all growth conditions except for M9 acetate where the cluster corresponding to termination occurring in the second and subsequent initiation in the third generation was chosen (Figures 8B and 8C; Figure S10). From clusters corresponding to termination and the previous initiation event it was possible to calculate C-periods for individual cells which could then be correlated with each cell's generation time calculated from $ln(2)/\lambda$ where λ is the growth rate acquired from fitting a single exponential to each cell's area expansion over time (Figure 8E). All of the corresponding clusters were used when calculating correlations. For Figure 8D these numbers were averaged and fit linearly before putting the x-axis scale to log scale.

The fork plots with multiple generations displayed in Figure 1A and Figure 3C were based on the creation of supercells as described above. Each generation in all supercells were then sorted and pooled together to visualize positions of fluorescent SeqA-Venus or YPet-DnaN foci along the cell long-axis. Offsets along the y-axis were calculated as the average offset in the supercells for each sorted generation. Furthermore, in Figure 3C only cells that were positioned at the trap constrictions were included in the supercells where each cell was required to be tracked for at least 5 minutes. Distributions of initiation areas for the supercells were fitted to a sum of five Gaussians for the P_{J23106}-*dnaA* strain and a sum of four Gaussians for the P_{lac}-*dnaA-mCerulean* strain.

In the experiments where DnaA expression was turned off (Figure 3 and Figures 4 E–G) fluorescence of mCerulean was used as a proxy of the concentration of DnaA. The fluorescence was quantified by measuring the pixel intensity in each cell, which were then average so that each cell had a specific intensity. Then, in Figure 3E, Figure 4G and Figure S8C the fluorescence intensities of the corresponding regions of interest for the reference strain and the strain carrying mCerulean were averaged. The reference strain average was then subtracted from the averages of the mCerulean strains. To determine the half-life of

bioRxiv preprint doi: https://doi.org/10.1101/2021.10.11.463968; this version posted October 11, 2021. The copyright holder for this preprint (which was not certified by peer review) is the author/funder, who has granted bioRxiv a license to display the preprint in perpetuity. It is made available under aCC-BY-NC-ND 4.0 International license.

mCerulean a single exponential was fit to the data points ranging from 10 minutes after image acquisition was restarted until the mCerulean signal plateaus.

For Figure 2B, Figures 3A–B, Figures 4D–F and Figures S8A–B fork plots were binned on time (bins not shown in Figure 4D). To create these detected fluorescent foci from each cell were sorted into each bin based on the time when they were detected relative to the start of the experiment. However, when calculating the average generation time cells that had less than 3 frames detected in a bin were put into the bin closest in time to be able to fit a single exponential to the area expansion over time as mentioned above. Births and divisions were registered in the bins where cells were born and divided. In Figure 2B cells were included in fork plots if they were tracked for at least 10 min while their parent and daughters had to be tracked for at least 5 min.

In all fork plots with one generation and without binning, cells were included if they were tracked for at least 10 min and their parent and daughters were tracked for at least 5 min. The exceptions to this were the fork plots where cells were grown in M9 acetate and RDM (Figure 5, Figure 8: Figure S10) where cells were included if they were tracked for at least 40 or 6.66 min while their parent and daughters had to be tracked for at least 20 or 3.33 min respectively.

For Figure 7 detected foci of YPet-DnaN and ParB-mCherry were tracked separately using the u-track algorithm, as described above. In order to estimate distances between YPet-DnaN and ParB-mCherry landmark-based registration of the fluorescence channels imaged on two different parts of the camera chip was performed. 100 nm fluorescent beads (TetraSpeck, Thermo Fisher) were imaged in both channels for the registration. Based on this registration fluorescent foci from the same cell detected in the two channels could be paired. Distances were estimated only between paired YPet-DnaN and ParB-mCherry foci that were the closest to each other. Additionally, each YPet-DnaN focus was only paired with one other ParB-mCherry focus for distance estimation.

The tracking of YPet-DnaN was also used to determine initiation and termination events. The termination events detected for each cell were used as a reference point to compare distances estimated over time in different cells (Figure 7B). Initiation and termination events were defined based on YPet-DnaN trajectories that were longer than 10 fluorescence frames. Additionally, the cell where the events were determined had to be detected for at least 40 phase contrast frames, it had to have a parent detected in at least 10 phase contrast frames as well as a sister and daughter cell that were detected in at least 3 phase contrast frames.

In the intensity based fork plots complete cell generations were selected based on the same criteria as in Figure 8. Camera pixel intensities were selected using the cell segmations mask as determined by phase contrast. Cells were aligned based on the angle of the vector pointing from the old to the new pole. The rotated fluorescence image of each cell in each fluorescence frame it was acquired in were binned according to cell area as determined by phase contrast images. For each area bin an average fluorescence image was constructed. The pixels located mid-cell along the cell short axis were extracted and plotted in fork plots.

bioRxiv preprint doi: https://doi.org/10.1101/2021.10.11.463968; this version posted October 11, 2021. The copyright holder for this preprint (which was not certified by peer review) is the author/funder, who has granted bioRxiv a license to display the preprint in perpetuity. It is made available under aCC-BY-NC-ND 4.0 International license.

Determination of *oriC/ter* ratio (NGS approach)

Overnight cultures of EL544 were grown in 1 ml medium (LB, succinate, and glucose) at 37 °C. The cultures were diluted at least 250 fold in 25 ml fresh media pre-heated to 30 or 37 °C and grown to OD_{600} = 0.2 (LB 30 and 37 °C), 0.17 (succinate 37 °C), and 0.14 (succinate and glucose 30 °C) where after rifampicin was added to the final concentration of 0.3 mg/ml and any ongoing transcription was allowed to terminate by leaving the cultures in the shaking incubator for 2 min before withdrawing 2x 1.5 ml samples. The cells in the withdrawn samples were quickly pelleted at room temperature and frozen at -84 °C (*i.e.* the cells were frozen within 4 min after adding rifampicin). In addition, 0.5 ml of a sample with stationary cells grown in LB at 37 °C for 1.5 days was pelleted and frozen. DNA was prepared using the MasterPure™ Complete DNA and RNA purification kit (Lucigen), according to the manufacturer's instructions. Illumina libraries were prepared using the TruSeq DNA PCR-Free library kit and the samples were sequenced using one lane of a MiSeq run. TrimGalore (https://www.bioinformatics.babraham.ac.uk/projects/trim_galore/) was used to remove adapter sequences and Bowtie2 (http://bowtie-bio.sourceforge.net/bowtie2/index.shtml) to map the sequencing reads over the reference genome of EL544. The genome position of the first base of each mapped read was binned into either ~30 kb or ~1.5 kb large binns.

Quantitative PCR

Experiment presented in Figure S6A: overnight cultures were grown in 1 ml medium supplemented with 1 mM IPTG (duplicates for EL562 and triplicates for EL1548). The cultures were diluted to 1:100 in 25 ml fresh pre-heated media supplemented with 1 mM IPTG and grown to OD_{600} = 0.2 where after samples for downstream RNA extraction were withdrawn (t_0). To mimic the medium switch in the fluidics experiment, the cells in the remainder of the cultures were carefully washed four times through centrifugation in media without IPTG. Then the cells were resuspended in 100 ml pre-heated medium and grown for four hours at 30 °C with shaking. Samples were withdrawn after 20, 40, 60, 120 and 240 min (i.e., t_1, t_2, t_3, t_4 and t_5).

Experiment presented in Figure S6B: quadruplicate overnight cultures were grown in 1 ml medium at varying IPTG concentrations (EL1548: 1, 0.05 and 0.005 mM). The cultures were diluted to 1:1,000 in 50 ml fresh pre-heated media supplemented with the same IPTG concentrations and grown to OD_{600} ≈ 0.2 when samples for downstream RNA extraction were withdrawn. However, the sample with 0.005 mM IPTG never seemed to reach OD_{600} = 0.2 although the overnight culture at the same concentration was fully grown. It was instead harvested after about 5 h. The samples with 0 mM IPTG were taken from the 1 mM cultures and treated similarly to the experiment presented in Figure S6A, although only one time point after switch was taken (240 min).

RNA from both experiments was prepared using the PureLink RNA Mini Kit (ThermoFisher) and DNase treated using the Turbo DNA-free kit (Invitrogen). The RNA was reverse-transcribed into cDNA through the High Capacity Reverse Transcription kit (ThermoFisher) and the Power SYBR Green PCR mix (ThermoFisher) was used for the

bioRxiv preprint doi: https://doi.org/10.1101/2021.10.11.463968; this version posted October 11, 2021. The copyright holder for this preprint (which was not certified by peer review) is the author/funder, who has granted bioRxiv a license to display the preprint in perpetuity. It is made available under aCC-BY-NC-ND 4.0 International license.

quantitative PCR reactions according to the manufacturer's instructions. Quantitative PCRs were performed in technical replicates on all samples, using primer pairs for *dnaA* and the two reference genes *cysG* and *hsaT*. After removing data from strange looking flat curves, the technical replicates were averaged and the fold change was calculated according to the $2^{-\Delta\Delta CT}$ method (Kenneth et al., 2001). The geometrical mean of the two reference genes was used in the calculations. Primers used in RT-qPCR are found in Table S4.

The samples used in the experiment presented in Figure S2 and Table S3 were the same as the ones prepared for the NGS Marker Frequency analysis. Quantitative PCRs were performed with 0.1 and 1 µl template and in technical duplicates for primer pair *ori 3* and single PCRs for primer pair *ter 14*. The technical replicates were averaged and the *ori*/*ter* ratio was calculated according to the $2^{-\Delta\Delta CT}$ method (Kenneth et al., 2001). Primers used in qPCR are found in Table S4.

Rifampicin (rif) run-out experiments

Overnight cultures (made in quadruplicates for the experiment in Figure S2 and duplicates for Figure S4) were diluted to grow for at least 10 generations in a shaking incubator before reaching $OD_{600} \approx 0.05$. To stop initiation and division, rifampicin and cephalexin were added to the final concentrations of 0.3 mg/ml and 10 mg/ml, respectively (from rifampicin stock 30 mg/ml in DMSO and cephalexin stock 10 mg/ml in H_2O). Since any ongoing replication is still active after adding the antibiotics, the replication forks will go on until termination allowing chromosome copy number to serve as a measurement of *oriC* number at the time point of adding the antibiotics. After 4–5 h of further incubation in the shaking incubator, 5 ml of the samples were fixed in 50 ml ice cold 70% EtOH and stored at -20 °C.

For flow cytometry analysis, cells in 1 ml aliquots of the stored samples were spun down and re-suspended in 1 ml of 50 mM Tris-Mg (pH 7.5) buffer supplemented with 10 mM $MgSO_4$. The cells were concentrated through centrifugation and 0.8 ml of the supernatant was removed. 1–2 *µ*l SYTOX green was added to stain the DNA in the cells and the DNA content in the fixed cells was analysed through a MACSquant Analyzer Flow Cytometer.

Growth rate determinations in plate reader

The measurements were performed by diluting overnight cultures grown in succinate medium 1:1,000 in fresh medium and thereafter the increase in optical density (OD_{600}) over time was measured using a Bioscreen C Reader (Oy Growth Curves) with shaking. Growth rates during the exponential phase were calculated and normalised to the growth of a reference strain included in the same experiment. For the experiment presented in Figure S7, the overnight cultures were grown in succinate medium supplemented with 0.01 mM IPTG and diluted in fresh media containing 1, 0.1, 0.01, or 0 mM IPTG.

bioRxiv preprint doi: https://doi.org/10.1101/2021.10.11.463968; this version posted October 11, 2021. The copyright holder for this preprint (which was not certified by peer review) is the author/funder, who has granted bioRxiv a license to display the preprint in perpetuity. It is made available under aCC-BY-NC-ND 4.0 International license.

Acknowledgements

We are thankful to our colleagues Jimmy Larsson, who performed some of the microfluidic experiments, and Spartak Zikrin, who worked on the analysis pipeline. We want to thank Irmeli Barkefors and Joakim Näsvall for helping us with the manuscript. We are also grateful to Rodrigo Reyes Lamothe for providing us with strains containing the YPet-DnaN construct and the DnaQ-YPet construct, to the Proteomics Core Facility at Sahlgrenska Academy, Gothenburg University, for performing the analysis for protein quantification, and to SciLifeLab in Uppsala for performing the Marker Frequency Illumina sequencing.

This study was made possible by grants from the ERC (Advanced grant no. 885360), the Swedish research council (grant no. 2016-06213 and 2018-03958), the Knut and Alice Wallenberg Foundation (grant no. 2016.0077, 2017.0291 and 2019.0439), and the eSSENCE e-science initiative.

The computations and data management was enabled by resources provided by the Swedish National Infrastructure for Computing (SNIC) at UPPMAX, partially funded by the Swedish Research Council through grant agreement no. 2018-05973.

References

Amir, A. (2014). Cell Size Regulation in Bacteria. Phys. Rev. Lett. *112*, 208102.

Atlung, T., and Hansen, F.G. (1993). Three distinct chromosome replication states are induced by increasing concentrations of DnaA protein in Escherichia coli. J. Bacteriol. *175*, 6537–6545.

Babic, A., Lindner, A.B., Vulic, M., Stewart, E.J., and Radman, M. (2008). Direct visualization of horizontal gene transfer. Science *319*, 1533–1536.

Baltekin, Ö., Boucharin, A., Tano, E., Andersson, D.I., and Elf, J. (2017). Antibiotic susceptibility testing in less than 30 min using direct single-cell imaging. Proceedings of the National Academy of Sciences 201708558.

Bates, D., and Kleckner, N. (2005). Chromosome and replisome dynamics in E. coli: loss of sister cohesion triggers global chromosome movement and mediates chromosome segregation. Cell *121*, 899–911.

Bremer, H., and Churchward, G. (1977). An examination of the Cooper-Helmstetter theory of DNA replication in bacteria and its underlying assumptions. J. Theor. Biol. *69*, 645–654.

Bremer, H., and Dennis, P.P. (2008). Modulation of Chemical Composition and Other Parameters of the Cell at Different Exponential Growth Rates. EcoSal Plus *3*.

Campbell, J.L., and Kleckner, N. (1990). E. coli oriC and the dnaA gene promoter are sequestered from dam methyltransferase following the passage of the chromosomal replication fork. Cell *62*, 967–979.

bioRxiv preprint doi: https://doi.org/10.1101/2021.10.11.463968; this version posted October 11, 2021. The copyright holder for this preprint (which was not certified by peer review) is the author/funder, who has granted bioRxiv a license to display the preprint in perpetuity. It is made available under aCC-BY-NC-ND 4.0 International license.

Campos, M., Surovtsev, I.V., Kato, S., Paintdakhi, A., Beltran, B., Ebmeier, S.E., and Jacobs-Wagner, C. (2014). A constant size extension drives bacterial cell size homeostasis. Cell *159*, 1433–1446.

Camsund, D., Lawson, M.J., Larsson, J., Jones, D., Zikrin, S., Fange, D., and Elf, J. (2020). Time-resolved imaging-based CRISPRi screening. Nat. Methods *17*, 86–92.

Cherepanov, P.P., and Wackernagel, W. (1995). Gene disruption in Escherichia coli: TcR and KmR cassettes with the option of Flp-catalyzed excision of the antibiotic-resistance determinant. Gene *158*, 9–14.

Christensen, B.B., Atlung, T., and Hansen, F.G. (1999). DnaA boxes are important elements in setting the initiation mass of Escherichia coli. J. Bacteriol. *181*, 2683–2688.

Datsenko, K.A., and Wanner, B.L. (2000). One-step inactivation of chromosomal genes in Escherichia coli K-12 using PCR products. Proc. Natl. Acad. Sci. U. S. A. *97*, 6640–6645.

Dennis, P.P., and Bremer, H. (1974). Macromolecular composition during steady-state growth of Escherichia coli B-r. J. Bacteriol. *119*, 270–281.

Donachie, W.D., and Blakely, G.W. (2003). Coupling the initiation of chromosome replication to cell size in Escherichia coli. Curr. Opin. Microbiol. *6*, 146–150.

Fujimitsu, K., and Katayama, T. (2004). Reactivation of DnaA by DNA sequence-specific nucleotide exchange in vitro. Biochem. Biophys. Res. Commun. *322*, 411–419.

Hansen, F.G., and Atlung, T. (2018). The DnaA Tale. Frontiers in Microbiology *9*.

Hansen, F.G., and Rasmussen, K.V. (1977). Regulation of the dnaA product in Escherichia coli. Mol. Gen. Genet. *155*, 219–225.

Hansen, F.G., Christensen, B.B., and Atlung, T. (1991). The initiator titration model: computer simulation of chromosome and minichromosome control. Res. Microbiol. *142*, 161–167.

Jaqaman, K., Loerke, D., Mettlen, M., Kuwata, H., Grinstein, S., Schmid, S.L., and Danuser, G. (2008). Robust single-particle tracking in live-cell time-lapse sequences. Nat. Methods *5*, 695–702.

Kasho, K., and Katayama, T. (2013). DnaA binding locus datA promotes DnaA-ATP hydrolysis to enable cell cycle-coordinated replication initiation. Proc. Natl. Acad. Sci. U. S. A. *110*, 936–941.

Katayama, T., Kubota, T., Kurokawa, K., Crooke, E., and Sekimizu, K. (1998). The initiator function of DnaA protein is negatively regulated by the sliding clamp of the E. coli chromosomal replicase. Cell *94*, 61–71.

Katayama, T., Kasho, K., and Kawakami, H. (2017). The DnaA Cycle in Escherichia coli: Activation, Function and Inactivation of the Initiator Protein. Front. Microbiol. *8*, 2496.

Kenneth, J., Livak, A., and Thomas, D. (2001). Schmittgen Analysis of Rela2 tive Gene Expression Data Using Real2Time Quantitative PCR and the 2-△△ C t Method. Methods *25*, 4022.

Kitagawa, R., Mitsuki, H., Okazaki, T., and Ogawa, T. (1996). A novel DnaA protein-binding

bioRxiv preprint doi: https://doi.org/10.1101/2021.10.11.463968; this version posted October 11, 2021. The copyright holder for this preprint (which was not certified by peer review) is the author/funder, who has granted bioRxiv a license to display the preprint in perpetuity. It is made available under aCC-BY-NC-ND 4.0 International license.

site at 94.7 min on the Escherichia coli chromosome. Mol. Microbiol. *19*, 1137–1147.

Knöppel, A., Andersson, D.I., and Näsvall, J. (2020). Synonymous Mutations in rpsT Lead to Ribosomal Assembly Defects That Can Be Compensated by Mutations in fis and rpoA. Front. Microbiol. *11*, 340.

Koskiniemi, S., Pränting, M., Gullberg, E., Näsvall, J., and Andersson, D.I. (2011). Activation of cryptic aminoglycoside resistance in Salmonella enterica. Molecular Microbiology *80*, 1464–1478.

Kurokawa, K., Nishida, S., Emoto, A., Sekimizu, K., and Katayama, T. (1999). Replication cycle-coordinated change of the adenine nucleotide-bound forms of DnaA protein in Escherichia coli. EMBO J. *18*, 6642–6652.

Lau, I.F., Filipe, S.R., Søballe, B., Økstad, O.-A., Barre, F.-X., and Sherratt, D.J. (2003). Spatial and temporal organization of replicating Escherichia coli chromosomes. Mol. Microbiol. *49*, 731–743.

Li, Y., Sergueev, K., and Austin, S. (2002). The segregation of the Escherichia coli origin and terminus of replication. Mol. Microbiol. *46*, 985–996.

Näsvall, J. (2017). Direct and Inverted Repeat stimulated excision (DIRex): Simple, single-step, and scar-free mutagenesis of bacterial genes. PLoS One *12*, e0184126.

Nielsen, H.J., Ottesen, J.R., Youngren, B., Austin, S.J., and Hansen, F.G. (2006). The Escherichia coli chromosome is organized with the left and right chromosome arms in separate cell halves. Mol. Microbiol. *62*, 331–338.

Pritchard, R.H., Barth, P.T., and Collins, J. (1969). Control of DNA synthesis in bacteria. In Symp. Soc. Gen. Microbiol, pp. 263–297.

Ranefall, P., Sadanandan, S.K., and Wählby, C. (2016). Fast adaptive local thresholding based on ellipse fit. In 2016 IEEE 13th International Symposium on Biomedical Imaging (ISBI), pp. 205–208.

Reyes-Lamothe, R., Sherratt, D.J., and Leake, M.C. (2010). Stoichiometry and architecture of active DNA replication machinery in Escherichia coli. Science *328*, 498–501.

Ronneberger, O., Fischer, P., and Brox, T. (2015). U-Net: Convolutional Networks for Biomedical Image Segmentation. In Medical Image Computing and Computer-Assisted Intervention – MICCAI 2015, (Springer International Publishing), pp. 234–241.

Schaper, S., and Messer, W. (1995). Interaction of the Initiator Protein DnaA of Escherichia coli with Its DNA Target *. J. Biol. Chem. *270*, 17622–17626.

Sekimizu, K., Bramhill, D., and Kornberg, A. (1987). ATP activates dnaA protein in initiating replication of plasmids bearing the origin of the E. coli chromosome. Cell *50*, 259–265.

Si, F., Le Treut, G., Sauls, J.T., Vadia, S., Levin, P.A., and Jun, S. (2019). Mechanistic Origin of Cell-Size Control and Homeostasis in Bacteria. Curr. Biol. *0*.

Taheri-Araghi, S., Bradde, S., Sauls, J.T., Hill, N.S., Levin, P.A., Paulsson, J., Vergassola, M., and Jun, S. (2015). Cell-size control and homeostasis in bacteria. Curr. Biol. *25*, 385–391.

bioRxiv preprint doi: https://doi.org/10.1101/2021.10.11.463968; this version posted October 11, 2021. The copyright holder for this preprint (which was not certified by peer review) is the author/funder, who has granted bioRxiv a license to display the preprint in perpetuity. It is made available under aCC-BY-NC-ND 4.0 International license.

Thomason, L.C., Costantino, N., and Court, D.L. (2007). E. coli genome manipulation by P1 transduction. Curr. Protoc. Mol. Biol. *Chapter 1*, Unit 1.17.

Wallden, M., Fange, D., Lundius, E.G., Baltekin, Ö., and Elf, J. (2016). The Synchronization of Replication and Division Cycles in Individual E. coli Cells. Cell *166*, 729–739.

Wang, P., Robert, L., Pelletier, J., Dang, W.L., Taddei, F., Wright, A., and Jun, S. (2010). Robust growth of Escherichia coli. Curr. Biol. *20*, 1099–1103.

Wiktor, J., Gynnå, A.H., Leroy, P., Larsson, J., Coceano, G., Testa, I., and Elf, J. (2021). RecA finds homologous DNA by reduced dimensionality search. Nature *597*, 426–429.

Yu, D., Ellis, H.M., Lee, E.C., Jenkins, N.A., Copeland, N.G., and Court, D.L. (2000). An efficient recombination system for chromosome engineering in Escherichia coli. Proc. Natl. Acad. Sci. U. S. A. *97*, 5978–5983.